Revision 1 #5018

Oriented Multiphase Needles in Garnet from Ultrahigh-Temperature Granulites, Connecticut, USA

Jennifer A. Axler[1] and Jay J. Ague[1,2]

[1]Department of Geology and Geophysics
Yale University
P.O. Box 208109
New Haven, CT 06520-8109 USA
jennifer.axler@yale.edu and jay.ague@yale.edu

[2]Peabody Museum of Natural History
Yale University
New Haven, CT 06511 USA

Abstract

This study investigates distinctive oriented, needle-shaped multiphase inclusions found within cores of garnets from felsic granulites of the Upper Member of the Bigelow Brook Formation and the Brimfield Schist (northeastern Connecticut, USA). The rocks crop out in the southern end of the Central Maine Terrane and thus are a part of the Acadian/Neoacadian Orogen. The typical mineral assemblage is: garnet + sillimanite + K-feldspar + plagioclase + quartz + cordierite + biotite±spinel. The sillimanite is commonly pseudomorphous after kyanite.

The multiphase needle inclusions and associated exsolved needles of rutile and ilmenite are mostly oriented parallel to <111> of garnet. The multiphase needles contain various combinations of quartz, micas, chlorite, rutile, graphite, a siliceous compositionally variable phase ("Phase-CV"), Zn-spinel, apatite, zircon, and rare ilmenite. We hypothesize that they represent inclusions of fluid that adhered to exsolving Ti±Fe oxide needles (mostly rutile) or extended along zones of weakness in garnet. This requires that multiphase needle formation occurred in response to cooling and/or decompression. The needles ultimately decrepitated during retrogression. We note that micaceous needle-shaped multiphase inclusions are rarely described; the closest analogs of which we are aware are found in UHP garnets of the Erzgebirge (Perchuk 2008).

The Brimfield Schist in this area underwent ultrahigh-temperature metamorphism (UHTM) of ~1000 °C at a minimum pressure of ~1 GPa (Ague et al. 2013). Here we provide new temperature estimates for the adjacent Upper Member of the Bigelow Brook Formation. Ternary feldspar reintegration using the activity model of Benisek et al. (2004) and Zr-in-rutile thermometry (Tomkins et al. 2007) give average temperatures of ~990 °C and ~1010 °C, respectively, at 1 GPa for this unit. Therefore, the recently discovered UHT zone in the Brimfield

Schist of northeastern Connecticut extends to the east to include the Upper Member of the Bigelow Brook Formation. Consequently, the first confirmed regional UHT locality in the United States is larger than initially recognized, and is at least 25 km long and 5–10 km wide. The oriented, elongate multiphase inclusions and petrographically-obvious oriented Ti±Fe oxide needles may be useful indicators of extreme temperature and/or pressure rocks in other field areas.

Introduction

Garnets and other refractory minerals in mantle rocks, ultra-high pressure (UHP) rocks, and high-grade gneisses may contain multiphase solid inclusions that are relicts of fluids entrapped during garnet growth (e.g., Stöckhert et al. 2001; van Roermund et al. 2002; Carswell and van Roermund 2005; Ferrando et al. 2005; Malaspina et al. 2006; Frezzotti et al. 2007; Perchuk 2008; Mposkos et al. 2009; Ferrero et al. 2012; Hermann et al. 2013). Common inclusion phases are quartz/coesite, feldspars, micas, chlorite, carbonates, apatite, rutile, graphite, and zircon. Microdiamond can also be found within these inclusions and by itself in garnet.

A growing number of multiphase inclusion localities have been recognized worldwide, but thus far none are in North America. Three examples are given here. **(1)** Multiphase inclusions ranging from ~5 to ~150 μm in diameter have been reported in garnet, orthopyroxene, and clinopyroxene from mantle-derived websterite in Fjørtoft, Norway (Carswell and van Roermund 2005). The inclusions generally contain Ti-phlogopite, kalsilite, Cr-spinel, magnesite, dolomite, Ba-Mg carbonate, Fe-Ni sulfide, Cl-apatite, rutile, zircon, and monazite; graphite or microdiamond are also found. The inclusions are interpreted to have formed from metasomatic fluids that infiltrated the peridotite. **(2)** Multiphase inclusions in garnets from UHP phengite-garnet-kyanite saidenbachite lenses of the Saxonian Erzgebirge (Bohemian Massif) are

composed mostly of phlogopite, quartz, paragonite, phengite, apatite, and rutile. In addition, graphite or microdiamond are common (Stöckhert et al. 2001, 2009). The inclusions record the presence of dense, alkali- and silica-bearing C-O-H fluids in deeply buried crust. **(3)** Multiphase inclusions in garnets within ultrahigh-temperature (UHT) granulites of the Barun Gneiss (Himalayas, Nepal) contain mostly quartz, biotite, muscovite, and plagioclase, together with accessory minerals such as zircon (Ferrero et al. 2012). The inclusions are crystallized anatectic melt trapped within the garnet host; similar inclusions from other localities may even preserve glassy quenched melt (Ferrero et al. 2012).

Rutile and ilmenite needles dominantly parallel to garnet <111> may accompany multiphase inclusions in garnet (Figs. 1 and 2). They are found predominantly in UHP rocks (e.g., Zhang and Liou 1999; Mposkos and Kostopoulos 2001; Zhang et al. 2003), >900 °C granulites (e.g., Snoeyenbos et al. 1995; O'Brien et al. 1997; Ague et al. 2013), and mantle rocks (e.g., Obata 1994; van Roermund and Drury 1998; Wang et al. 1999; van Roermund et al. 2000). The rutile needles have anomalous (non-parallel) extinction (Griffin et al. 1971). This reflects single or multiple definite crystallographic orientation relationships (COR) between rutile and host garnet that are now well characterized by electron backscatter diffraction and transmission electron microscope studies (Proyer et al. 2013; Hwang et al. 2014).

The concentration of Ti in aluminous garnet is generally higher at higher pressures (*P*) and/or higher temperatures (*T*), although there is considerable variation and Ti-*P*-*T* relationships are complicated (e.g., Khomenko et al. 1994; Ono 1998; Massonne and Brandelik 1998; Zhang and Liou 2003; Zhang et al. 2003; Kawasaki and Motoyoshi 2007; Hermann and Spandler 2008; Konzett and Frost 2009; Auzanneau et al. 2010; Proyer et al. 2013). Ti generally is thought to go

into the octahedral site of garnet, but can also enter the tetrahedral site (e.g., Malitesta et al. 1995, Massonne and Brandelik 1998; Ackerson et al. 2013; Proyer et al. 2013).

The conventional interpretation of the oriented Ti±Fe oxide inclusions is that during cooling and exhumation the Ti is no longer stable in the garnet structure and thus it exsolves (precipitates) out along a preferred crystallographic direction(s) (e.g., Haggerty 1991; Zhang and Liou 1999; Ye et al. 2000; van Roermund et al. 2000; Snoeyenbos and Koziol 2008; Ague and Eckert 2012). For example, Proyer et al. (2013) concluded that the complex but definite COR between oriented rutile needles and garnet host from UHP metapelite (Greek Rhodope) reflected a precipitation origin. Ague and Eckert (2012) documented Ti-depleted haloes in garnet surrounding Ti±Fe oxide crystals in 1000 °C granulites from the field area studied herein, thus confirming a precipitation origin for these particular rocks. We note in this context that the lack of local Ti depletion halos in garnet is not a refutation of precipitation hypotheses as it may simply mean that garnet lost most of its Ti due to extensive needle formation. In addition, halos could be obscured if, subsequent to precipitation, there was continued Ti diffusion in garnet or recrystallization of garnet.

Other needle formation processes could potentially operate (see review in Proyer et al. 2013). For example, unusual Idaho "star" garnets (Guinel and Norton 2005), well known among mineral and gem enthusiasts for their four-star or six-star asterism, have rutile needle inclusions that may have formed by precipitation from garnet or co-precipitation of rutile and garnet (Hwang et al. 2014). Star garnets are rare. They are known from only a handful of localities worldwide—most famously Idaho and India—but also Madagascar, Sri Lanka, Tanzania, and North Carolina (Schmetzer et al. 2002). Star garnets are not considered further herein given their unusual nature and because of uncertainties regarding peak metamorphic *P*-*T* conditions.

The shapes of multiphase inclusions vary. They are commonly rounded, "boxy", or have a negative crystal shape. In addition, the oriented multiphase *needle* is a rarely-described inclusion type that is typically associated with Ti ± Fe oxide needles in UHP rocks. For example, Ye et al. (2000) describe composite rutile-apatite needles in garnet from eclogite within the Sulu UHP metamorphic belt (China). Ruiz-Cruz and de Galdeano (2013) report multiphase rutile-apatite needles and rutile-silicate rods in garnet from UHP granulites (Ceuta, northern Africa). The only reported occurrence of oriented multiphase needles that contain micas of which we are aware is in the diamondiferous Erzgebirge rocks (Perchuk 2008).

We report on a newly-discovered locality for oriented multiphase needles in garnet (northeastern Connecticut, USA; Fig. 3). They are found parallel to <111> in garnet and are associated with, and parallel to, oriented rutile and ilmenite needles (Figs. 1 and 2). They generally contain phlogopite, quartz, and rutile; other phases that may be found include: graphite, phengite-muscovite, ilmenite, apatite, monazite, Zn-spinel, zircon, and a siliceous, compositionally variable phase (herein termed Phase-CV to denote compositional variability). The advent of field emission gun electron probe microanalyzer (FEG-EPMA) technology facilitates quantitative analysis of oxide needles and tiny inclusion phases impossible with standard EPMA methods. The high Zr contents of the rutile needles, together with ternary feldspar compositions from nearby localities, unequivocally indicate ultrahigh-temperature metamorphism (UHTM). This finding expands the newly-discovered UHT area of northeastern Connecticut (Ague et al. 2013) to the north and east. Our results document textural relationships that bear on deep metamorphic processes and that may be useful in identifying extreme *T* and/or *P* rocks in other field areas.

Geology

The oriented rutile, ilmenite, and multiphase inclusions were discovered in garnets from sillimanite-rich metapelitic gneisses within the Brimfield Schist and the Upper Member of the Bigelow Brook Formation (UM-BBF) of the southern end of the Central Maine Terrane (CMT; Fig. 3). The UM-BBF consists predominantly of sulfidic rusty-weathering gneiss and schist. The lenses of sillimanite-rich rock occur throughout and typically contain: garnet + sillimanite + K-feldspar + plagioclase + quartz + cordierite + biotite. Rutile, ilmenite, graphite, apatite, monazite, zircon, rare spinel, and pyrrhotite are accessory phases. These rocks are discernible from the surrounding schist and gneiss as they form small ridges and contain megacryst pseudomorphs of sillimanite after kyanite up to 10 cm long (Fig. 4a, Peper and Pease 1975). The Brimfield Schist is similar and consists mostly of metapelitic and quartzofeldspathic gneisses, but also includes pods and layers of calc-silicates and metamorphosed mafic and ultramafic rocks (Ague et al. 2013). Probable sillimanite pseudomorphs after kyanite are present but less obvious, perhaps due to stronger deformation and recrystallization.

The early history of the northern domain of the CMT in New Hampshire, Maine, and Massachusetts differs from that of the southernmost domain in Connecticut (CT). The northern domain records sillimanite pseudomorphs after andalusite (Chamberlain and Lyons 1983; Thomson 2001), whereas the southern domain contains sillimanite pseudomorphs after kyanite (Fig. 4a; Peper and Pease 1975; Fahey and Pease 1977). Thus, the first preserved prograde metamorphism occurred at different conditions within the CMT.

UHTM conditions for the Brimfield Schist (Fig. 3) were at least ~1000 °C and ~1 GPa (see Ague et al. 2013 for pseudosection, *P-T* estimates, and path). The kyanite pseudomorphs could be evidence of either high pressures at high temperatures (≥~1.4 GPa; 1000 °C) or growth at moderate crustal pressures in the amphibolite facies followed by heating to UHT conditions.

Pseudosection analysis gives the minimum *P* of ~1 GPa for the quartz-absent assemblage garnet + K-feldspar + Al_2SiO_5 + rutile + melt at 1000 °C. If quartz was present then the minimum *P* estimate is ~1.4 GPa, consistent with kyanite stability at these temperatures. The *P*-*T* path subsequent to UHTM involved: cooling to around 800 °C at 0.5–0.6 GPa, followed by reburial which brought the rocks back into the kyanite stability field at 0.8–0.9 GPa and ~600 °C. The reburial is evidenced in the field area by variably-developed overprinting of the Brimfield Schist with kyanite (e.g., Ague 1995; Thomson 2001); overprint kyanite has yet to be recognized in the UM-BBF.

The field area is cut by a series of westward dipping faults that are generally interpreted to be thrusts (Fig. 3; Peper and Pease 1975; Fahey and Pease 1977; Rodgers 1981). The easternmost of these (Eastford fault) cuts the 379 Ma Canterbury Gneiss, thus establishing a maximum age for fault movement (U-Pb zircon dating of Wintsch et al. 2007). The CMT of northeastern CT underwent high-grade metamorphism during Acadian/Neoacadian orogenesis (Devonian; Rodgers 1981; Robinson and Tucker 1982; Schumacher et al. 1989; Armstrong et al. 1992; Wintsch et al. 1992; Robinson et al. 1998; Thomson 2001; Wintsch et al. 2009); however, the precise timing of events awaits future geochronological studies.

Methods

Wavelength-dispersive spectrometer (WDS) analyses, energy-dispersive spectrometer (EDS) analyses, and backscattered electron (BSE) images were acquired using the JEOL JXA-8530F field emission gun electron probe microanalyzer (FEG-EPMA) and Probe for EPMA software at Yale University. Natural and synthetic standards were used together with $\phi - \rho - z$ matrix corrections. Off-peak background corrections were used for most phases. In addition, the mean atomic number (MAN) background correction procedure was used for several mica and

Phase-CV analyses to reduce exposure time and therefore reduce beam damage (e.g., Donovan and Tingle 1996).

Quantitative analyses of oxides and hydrous phases were done at 10 kV. The low kV reduces beam damage of hydrous phases, and allows quantitative analysis of small (<2–10 μm) oxide grains due to the small activation volume of ~1 μm^3. The beam was focused for oxides, and defocused to as much as 20 μm for hydrous phases and feldspars. 15 kV was used for garnet and feldspars. The current of the electron beam depended on the beam sensitivity of the mineral being analyzed; 150 nA for oxides and garnet and 2.5–10 nA for micas, Phase-CV, and feldspars. Major elements were counted for 10–40 s on peak; key trace elements were counted for long times (100–200 s on peak) to optimize counting statistics. A high-reflectivity PETL crystal was used to gather Ti (in garnet) and Zr (in rutile) counts. Analytical uncertainties are discussed in Ague and Eckert (2012).

Chemical mapping of phosphorus in garnet was done using WDS at 15 kV and 150 nA with a 150 ms dwell time. Maps of the acicular multiphase inclusions were made using EDS (Si in Fig. 7d) or WDS (all others) at 10 kV and 15 nA with dwell times ranging from 30 to 50 ms.

Temperatures (*T*) were estimated using Zr-in-rutile thermometry and ternary feldspar thermometry. We used the Zr-in-rutile thermometer calibration of Tomkins et al. (2007) (Table 1). For ternary feldspar thermometry, antiperthite compositions were reintegrated following Ague et al. (2013); the *T* estimates used the feldspar activity models of Benisek et al. (2004, 2010). The method estimates the *minimum T* for the crystallization of homogeneous ternary feldspar.

To estimate the original bulk Ti content of a garnet containing oriented rutile and ilmenite needles (section JAQ124A-6), a grid of 25 μm diameter spot analyses was done in a rutile and

ilmenite needle-rich region of its core following the method outlined in Ague and Eckert (2012). As the oxides are precipitates out of the garnet, a wide beam was used to combine the Ti content of the oxide needles with the Ti content remaining in the garnet to determine the garnet's original composition before oxide precipitation. Four adjacent domains were selected to evaluate the variability of the garnet Ti content; they contained 94, 143, 59, and 160 spot analysis points.

Electron backscatter diffraction (EBSD) work was done using an XL-30 ESEM-FEG operating at 20 kV and 3 nA. The Kikuchi patterns were indexed using Channel 5 software by Oxford Instruments HKL. The crystallographic orientation of garnet was determined to verify the shape preferred orientation of oxide and multiphase needles along garnet <111> (Fig. 2).

Petrographic Relationships

The multiphase-needle-bearing garnets are typically about 0.25 to 1 cm in diameter. They are rich in pyrope (25–30%) and almandine, but poor in grossular and spessartine (Table 2). The multiphase-needles and Ti±Fe oxide-needles mostly lie parallel to <111> (as verified by EBSD; Fig. 2), and occupy domains within garnet cores (Figs. 1, 4c, and 5). Needle lengths range from about 10 to 125 μm. The rutile needles are the thinnest and are typically 0.5 to 3 μm in diameter. The ilmenite needles tend to be thicker (~6 μm diameter). The multiphase-needles are distinguished by their translucence and rough outlines (Figs. 1b and 2).

The garnet cores are surrounded by rims that lack oriented needles but that commonly contain sillimanite inclusions (Fig. 5a). Core-rim boundaries range from diffuse to sharp; sharp boundaries are quite common (Figs. 4c and 5). At most localities, sillimanite inclusions in garnet rims are roughly parallel to the surrounding foliation (see Ague and Eckert 2012; Ague et al. 2013). However, at and around site 124 the sillimanite prisms are arranged in a roughly radial

229 way around sharply-defined garnet cores (Fig. 5a), whereas matrix sillimanite is parallel to the
230 foliation and defines a lineation.

231 Most of the multiphase needles have cracks radiating out of their corners (Fig. 6); these
232 cracks produce the rough outlines observed petrographically (Fig. 2). The lengths of the radiating
233 cracks can exceed the diameter of the inclusion from which they originated. The cracks are
234 generally filled with hydrous minerals such as chlorite or phlogopite. Depending on orientation,
235 the needles may intersect the garnet surface at a point if they are nearly perpendicular to the
236 plane of the thin section (e.g., Figs. 6a–6g), or be more elongate if they lie sub-parallel to the
237 plane (e.g., Figs 6h, 6i, 7a, and 7b). The multiphase inclusions generally have a near-hexagonal,
238 "negative" crystal shape in cross section when viewed perpendicular to the elongation direction
239 (e.g., Figs 6a-6d, 6f, 6g, 7c, and 7d).

240 Phlogopite + quartz ± rutile are the most abundant minerals in the multiphase inclusions.
241 Muscovite/phengite is less abundant but is still widely observed. Multiple mica phases are
242 commonly intergrown (Figs. 6 and 7b; see below). Rare chlorite may be present together with
243 the micas or in cracks. Graphite plates and rods that give pure carbon EDS spectra are common
244 (Fig. 6c); isolated graphite inclusions can also be found throughout garnet. "Phase-CV" is silica-
245 rich and compositionally variable. It is likely composed of amorphous material or
246 nanocrystalline minerals too small for separate analyses. Other minerals found in the multiphase
247 inclusions are: apatite, monazite, Zn-spinel, zircon and ilmenite. The long axis of rutile and the
248 cleavage trace of phlogopite are commonly parallel to the elongation direction of the entire
249 inclusion, although this isn't always the case (Figs. 6 and 7).

250 The kyanite pseudomorphs are blue-gray, prismatic, and predominantly oriented within
251 the foliation. Rare spinel is found as inclusions in the pseudomorphs in several samples from the

124 sample area (Fig. 4b). This spinel has an unusual "wormy" appearance in some ways similar to myrmekite; however the long axes of the spinel blebs are usually aligned with the long-direction of the sillimanite. The spinel inclusions are most elongate in the central parts of the inclusion clusters, and become more equant on the margins (Fig. 4b). Ilmenite inclusions are also found with spinel. The texture of the spinel inclusions does not suggest overgrowth by sillimanite, but rather some other mechanism associated with the conversion of kyanite to sillimanite. One possibility is that the oxide phases were produced from impurities originally present in the kyanite that crystallized when the pseudomorphs formed.

Mineral Chemistry

Garnet

The major elements show relatively little zonation due to diffusive smoothing at granulite facies conditions (Figs. 8a-c; e.g., Kohn 2014), although retrograde drops in Mg/Fe were noted at contacts with biotite or cordierite. In general, Ca preserves the greatest degree of internal zonation for major elements; however, the variations are relatively small, ranging from about 0.11 to 0.16 atoms per formula unit (afu per 12 O) Ca (Fig. 8c).

The trace elements Ti, P, Y, and Na record distinct zonation within the garnets. For example, in Figure 8d, the Ti content of the garnet drops and flattens as the profile crosses into the oxide needle-rich core. This is likely due to Ti diffusing out of the garnet to form the rutile and ilmenite needles in the core region (e.g., Ague and Eckert 2012; see below). Phosphorus is elevated within needle-rich garnet cores with an average of ~0.004 afu P. (Figs. 8e, 9b, and 9c). Core-rim boundaries are typically marked by a drop in P content; P may then increase toward the rim but concentrations do not reach core values. Notably, the phosphorus preserves overprint zonation (e.g., Ague and Carlson 2013), easily seen in a chemical map of garnet, but also shown

in garnet profiles as steep drops in concentration (Figs. 9b and 9c). The preservation of sharp gradients in P concentrations demonstrates that much of the original chemical growth zonation is retained even at UHT conditions, and has not been erased by diffusion, recrystallization, or dissolution-reprecipitation. Yttrium contents are typically largest in garnet cores (~0.004-0.006 afu Y) and decrease toward rims. This trend can be seen in the garnet profile of Figure 8f. Some garnets have measureable zoning in Na, with the largest concentrations in garnet cores (Fig. 9a). In summary, the largest concentrations of most trace elements are found in the garnet cores, especially in the areas which contain multiphase and oxide needles.

The oriented Ti±Fe oxide needles almost certainly precipitated from Ti-bearing garnet (e.g., Ague and Eckert 2012; Proyer et al. 2013). Therefore, the combined Ti content of the Ti±Fe oxide needles and the garnet likely reflects the Ti content of the garnet immediately prior to Ti±Fe oxide precipitation. To measure the bulk Ti content, wide-beam (25 μm) spot analyses were spread over a grid in the needle-rich core of JAQ 124A as described in the Methods section. The four analyzed domains contain average TiO_2 concentrations of 0.193 (n=94), 0.091 (n=143), 0.111 (n=59), and 0.129 (n=160) wt. %; the average of all 408 spot analyses is 0.13 wt. %. It is unclear if these values reflect the maximum garnet Ti content at peak conditions, because Ti can diffuse through garnet at extreme temperatures (Ague and Eckert 2012). Thus, the original Ti distribution could have been diffusionally modified to some extent prior to needle precipitation. The garnet within the analyzed grid domains also contains appreciable amounts of P_2O_5 (~0.07 wt. %) and ZrO_2 (~150 ppm).

Rutile

Rutile needles in garnet and rutile grains from the matrix were analyzed from the 124 sample locality (Table 1). Rutile needle chemistry is independent of distance from quartz

inclusions or whether or not the needle is within a multiphase inclusion. The rutile needles in garnet cores are remarkably Zr rich, containing ~1.1 wt. % ZrO_2 on average. In contrast, matrix rutile grains have an average of ~580 ppm ZrO_2. Rutile also contains variable amounts of minor and trace elements including Fe, V, Ta, Nb, and Cr. Fe concentrations tend to be greater in Zr-rich rutile crystals.

Sheet silicates

Representative analyses of micas within the oriented multiphase inclusions are given in Table 3. Phlogopite has relatively low Ti contents and is quite Mg-rich ($Mg/[Mg+Fe^{2+}] \sim 0.8$). This may reflect low-*T* re-equilibration, as biotite Fe/Mg and Ti contents generally decrease with decreasing *T*. One very unusual characteristic of some phlogopites are high Ni contents in excess of 2.5 wt. %. High-Ni phlogopites also have significantly higher concentrations of Cr, Ca, and Ba than low-Ni grains. These cannot be analytical artifacts due to some sort of unrecognized beam overlap onto other phases because there are no Ni-, Cr-, or Ba-rich phases in the inclusions, and Ca-rich silicates are rare. The needles lost fluid when they decrepitated (see below), so phlogopite halogen contents were likely reset. Nonetheless, one analyzed phlogopite (Phl-3) retains ~1.3 wt. % F; such elevated concentrations probably act to stabilize mica at UHT conditions (Kelsey and Hand 2014). The percentages of Na on the interlayer sites of the analyzed white micas is considerable (~25–50 mol %). The phengite component can exceed 3.2 Si per 11 O. White mica $Mg/[Mg+Fe^{2+}] \sim 0.5$ is significantly less than that for phlogopite.

The micas are commonly either too fine grained or too intergrown to get an individual analysis. The structural formulas for intergrown micas in Table 3 obviously do not represent a single phase. However, they illustrate that the sums of tetrahedral, octahedral, and interlayer sites are consistent with micas and, thus, other phases are unlikely in the composite analyses.

Phase-CV

Phase-CV is generally found in patches <10 μm in diameter (Figs. 7c and 7d). It is rich in Si and, in most cases, Al, but the amounts of K, Na, and Ca relative to Si and Al are too low for feldspar (Table 4). A hydrous volatile component is almost certainly present as most totals are <99 wt. %. Phase-CV may originally have had a larger water content that was lost through decrepitation, H_2 diffusion through garnet, reactions to produce hydrous inclusion sheet silicates, or leakage via dislocations (Frezzotti et al. 2007). Concentrations of Fe, Mg, Mn, and Ni are low and variable. Chemical mapping demonstrates that patches of Phase-CV can be remarkably compositionally heterogeneous on micron/submicron scales (Figs. 7c and 7d).

Spinel and ilmenite

Spinel and ilmenite are found together in sillimanite (Fig. 4b); representative chemical analyses are given in Table 5. The spinel is dominated by hercynite, but also contains significant Mg-spinel (~30%) and ghanite components (~15%). Ilmenite is relatively pure although structural formula calculations indicate the presence of some Fe^{3+}.

Thermometry and UHTM

Zr-in-rutile thermometry

Using the Zr-in-rutile thermometer of Tomkins et al. (2007), we estimated the equilibration temperature of rutile assuming equilibrium with quartz and zircon (Table 1). Small zircon inclusions are widespread throughout the garnets. We note that if there was any degree of zircon undersaturation, then the resulting temperature estimates would be minima. There was no variation in Zr content with proximity to quartz. Quartz is an abundant inclusion within garnet and its activity should not vary significantly throughout the garnet to affect the temperature estimates.

The average *T* estimate for rutile needles within garnet cores for site 124 in the UM-BBF is 1008 °C ± 11 (2 σ) assuming a pressure (*P*) of 1.0 GPa as given by the *P-T* history of the Brimfield Schist determined in Ague et al. (2013). The mean temperature estimate of ~1010 °C is unequivocally UHT; varying *P* by ± 0.4 GPa changes the value by only ± 27 °C. In addition, this estimate would be a minimum if some degree of cooling was required to precipitate the Ti±Fe oxides. We note that the rutile needle with the highest Zr content and therefore the highest temperature estimate (~1.3 wt. % ZrO_2; ~1030 °C) was found in an oriented-multiphase inclusion coexisting with quartz (Fig. 6b). This is strong evidence that multiphase needle formation took place at ultrahigh temperatures.

The average Zr content of matrix rutile is much lower than that of rutile needles in garnet cores, likely due to re-equilibration during cooling (e.g., Luvizotto and Zack 2009; Jiao et al. 2011; Ague et al. 2013; Ewing et al. 2013). Pressures were probably in the range 0.5–1.0 GPa (Ague et al. 2013). The low Zr contents require equilibration under sub-UHT conditions; average values of 680 °C to 705 °C are obtained for the analyses in Table 1 at representative pressures of 0.5 and 1.0 GPa, respectively.

Ternary feldspar thermometry

Rutile needles in garnet are too thin for quantitative analysis at sites 167 and 172, but rocks from both localities contain antiperthite suitable for ternary feldspar thermometry (Fig. 4d). The temperature estimates for antiperthites from samples 167 and 172 range from 921 - 1005 °C using the feldspar activity models of Benisek et al. (2004, 2010). The antiperthites record UHT conditions regardless of the feldspar activity model used (Table 6). Thus, evidence for UHTM is preserved at multiple localities within the UM-BBF.

Comparison to Other Multiphase Inclusions

Multiphase inclusions in the UHP diamond-bearing saidenbachite of the Erzgebirge, Germany, have some features that are similar to the multiphase needle inclusions found in Connecticut (CT). For example, Stöckhert et al. (2001, 2009) describe multiphase inclusions with radiating cracks and hexagonal negative crystal garnet shapes that resemble the cross-section of the CT inclusions perpendicular to their elongation direction (e.g., Figs. 6a-g). The cracks are considered a result of brittle failure of the garnet host due to internal fluid overpressure generated within the inclusions during exhumation. Both localities' inclusions contain quartz, phlogopite, white mica, rutile, chlorite, apatite, zircon, and graphite (see Fig. 3 of Stöckhert et al. 2001). Microdiamond and paragonite are present in the Erzgebirge inclusions, whereas the CT inclusions contain graphite and phengite-muscovite with as much as 50% paragonite component (Table 3). A critical difference is that the CT inclusions are acicular and oriented along garnet <111>, whereas the Erzgebirge inclusions of Stöckhert et al. (2001, 2009) are roughly equant.

Oriented multiphase needles *are* found, however, in the sample of diamondiferous Erzgebirge saidenbachite studied by Perchuk (2008). This is the only other example of oriented micaceous multiphase needles of which we are aware. The Erzgebirge needles contain rutile and two other phases thought to be phlogopite and paragonite, are crystallographically oriented with respect to their garnet host, and are similar in size to the CT needles (several μm wide, up to 200 μm long). From Perchuk's (2008) Figures 2 and 3, it is unclear if the Erzgebirge needles have filled radiating cracks; therefore, they may not have decrepitated like the CT needles. The Erzgebirge needles are concentrated radially in halos around large (~200 μm), non-acicular multiphase inclusions that contain quartz, phengite, chlorite, rutile, and apatite and that are inferred by Perchuk (2008) to have decrepitated. The CT multiphase needles do not surround

large multiphase inclusions, but rather are found concentrated in discrete areas within garnet cores (Fig. 5). Erzgebirge garnet can also contain oriented, single-phase rutile needles (e.g., Fig. 1a in Ague and Eckert 2012).

Ferrero et al. (2012) describe crystallized and glassy melt inclusions in garnet from three different granulite localities (Kerala Khondalite Belt, India; Ronda migmatites, Spain; and Barun Gneiss, Nepal Himalaya). Their melt inclusions are found in clusters, although, unlike the CT examples, the clusters are not always present in garnet cores. A negative crystal shape is common for the inclusions, similar to the cross-section perpendicular to the elongation direction of the CT inclusions. However, the Ferrero et al. (2012) inclusions are generally equant while the multiphase inclusions in our rocks are acicular. Phases commonly found within the Ferrero et al. (2012) inclusions are: quartz, plagioclase, K-feldspar, biotite, muscovite, and glassy material. As in our rocks the muscovite and biotite generally grow adjacent to each other resulting in interlocking crystals. On the other hand, the CT inclusions lack feldspars. Ferrero et al. (2012) also found a few elongate, unoriented, tubular melt inclusions which have diameters of 5-6 μm and lengths less than 100 μm. They interpreted these to be the result of melt adhering to elongate phases such as rutile.

Original Nature of the Multiphase Inclusions

We consider it likely that the needles originated as fluid inclusions of hydrous melt, aqueous fluid containing dissolved silicate material, or some combination of these that were trapped in growing garnet. Supercritical fluids intermediate between aqueous fluids and hydrous melts are another possible fluid type. These fluids, however, are likely stable only under UHP conditions (e.g., Manning 2004; Ferrando et al. 2005; Hermann et al. 2013) and we have found no evidence to date that the CT rocks are UHP.

As described above, the phases in the CT inclusions have textural relationships similar to those of fluid inclusions recognized elsewhere; these include angular wedge-like protrusions of one phase into another (Fig. 6a) and granophyre-like quartz-mica intergrowths (Fig. 6g; e.g., Ferrero et al. 2012; Stöckhert et al. 2001, 2009). In addition, the quartz and mica-bearing phase assemblages in the CT inclusions are similar to those observed in other well-documented examples. Moreover, the presence of siliceous "Phase-CV", which is probably glassy material or its nanocrystalline equivalent, is also consistent with a fluid origin. The common occurrence of graphite demonstrates that carbon was present in the CT inclusion fluids.

The roughly 30–50 volume percent micas + hydrous Phase-CV in the inclusions yields H_2O contents of 1–2 wt.%. Original water contents were potentially greater but are difficult to constrain as water loss may have occurred via decrepitation and diffusion.

It is possible that Phase-CV represents relic trapped hydrous melt. However, most Phase-CV analyses do not correspond to any common type of igneous melt and have normative quartz >60 wt.%, well above the normal SiO_2 limit for igneous rocks (Fig. 10). All have normative corundum. Three of the analyses are tonalitic, which is unexpected as the host rocks contain K-feldspar (MI-1 and MI-2 in 124A-2, Table 4). Compositions vary widely between inclusions in a single sample; for example, those in 124A-6 span the range from tonalitic to extremely quartz rich (Fig. 10). It is possible that the compositions of Phase-CV diverge from "normal" melt due to crystallization of minerals within the inclusions, reaction of those minerals with melt subsequent to their crystallization, or reaction of melt with the garnet host. It is also possible that Phase-CV compositions were modified by diffusion of elements through garnet (e.g., Proyer et al. 2013). For example, alkali and alkaline earth loss could have led to high normative corundum, and low normative feldspars.

436 The analyzed Phase-CV material from sample 141B (Table 4) is noteworthy because it
437 contains multiple compositional domains: one is extremely siliceous (MI-2a) whereas the others
438 are still highly siliceous but contain more Al and Ca (MI-2b, 2c; Fig. 10). The internal variability
439 of Phase-CV is also clear in the chemical maps of other inclusions from this sample (Fig. 7c) and
440 elsewhere (Fig. 7d). Remarkably, the different compositional domains can be intergrown on
441 micrometer to submicrometer scales. The BSE image reveals that the inclusions in sample 141B
442 may contain visible porosity which suggests the former presence of fluid (Fig. 7c). We speculate
443 that the 141B Phase-CV material may be quenched aqueous fluid that contained substantial
444 dissolved silicate material, or some combination of such a fluid and hydrous melt. This is
445 consistent with the high silica content, but not the lack of alkalis (e.g., Manning 2004, 2013).
446 One possibility is that the alkalis were lost together with fluid along cracks via decrepitation, or
447 by diffusion through garnet.

448 The absence of discernable crystals in Phase-CV demonstrates impeded crystal
449 nucleation and growth. Cesare et al. (2009) attribute the lack of crystallization observed in melt
450 inclusions in metamorphic garnets to surface free energy effects associated with small pores.
451 Small (nanometer to micrometer scale) crystals have higher interfacial energy and thus decreased
452 stability relative to larger ones. It follows that smaller pore (inclusion) sizes that restrict crystal
453 size and radius of curvature will increase the level of saturation necessary for precipitation (e.g.,
454 Putnis et al. 1995; Emmanuel and Ague 2009; Emmanuel et al. 2010).

455 **Possible Mechanisms of Multiphase Needle Formation**

456 We consider several hypotheses for the formation of multiphase needle inclusions.
457 Additional general mechanisms for oriented inclusion formation not discussed herein are
458 considered unlikely based on the arguments of Proyer et al. (2013).

459 **Hypothesis 1: Trapped fluid inclusions**

460 Our preferred hypothesis is that the multiphase needles formed due to physical interaction
461 between fluid inclusions and exsolving rutile needles. Most of the oriented rutile and ilmenite
462 needles are not in contact with another inclusion phase, although they are more abundant in areas
463 where the multiphase needles are present. This demonstrates that the Ti±Fe oxide needles did not
464 crystallize from fluid, but instead exsolved out of garnet. The key questions then become: why
465 are the inclusions acicular, and why are they crystallographically oriented?

466 We postulate the series of events illustrated in Figure 11. The first step requires fluid to
467 be entrapped within a growing, Ti-bearing garnet (Fig. 11a). Later, during retrogression, the
468 Ti±Fe oxide needles exsolved out of the garnet due to cooling and/or decompression (Fig. 11b).
469 Garnet contains Ti sufficient for Ti±Fe oxide needle formation because it formed at ≥1000 °C
470 and high *P* as well (at least 1 GPa).

471 Two processes may have come into play during Ti±Fe oxide precipitation. The first
472 involves the growth of exsolved Ti±Fe oxide needles that intersect fluid inclusions allowing the
473 fluid to adhere to the oxide needles and elongate (Fig. 11b). A second possible process occurring
474 simultaneously is the movement of fluid solely due to internal overpressure within the inclusion.
475 During exhumation, the pressure on the rock mass is reduced. However, the inclusions within a
476 robust host such as garnet will retain a higher pressure (close to that of entrapment) than the rock
477 mass (e.g., Stöckhert et al. 2001, 2009). To reduce the overpressure within the inclusion the fluid
478 could propagate along a direction of weakness in the garnet—{110} partings that intersect to
479 define <111>. During this process the overpressure of the inclusion is not sufficient to crack the
480 garnet and decrepitate, but can cause elongation. As the fluid moves within the garnet it may or
481 may not intersect Ti±Fe oxide needles.

The first process of fluid adhering to oxide needles as they grow and intersect the melt inclusions is considered the main cause of elongation because most inclusions contain rutile needles parallel to their elongation direction. The nucleation of Ti±Fe oxides may have been aided by presence of the fluid inclusions. The interface between fluid inclusions and the garnet host would provide a surface on which heterogeneous nucleation may more readily take place than in the lattice of the host, as heterogeneous nucleation has a lower free energy barrier to overcome. In addition, defects in the garnet crystal lattice surrounding fluid inclusions would lower the free energy of nucleation and could aid the exsolution of rutile (e.g. Cahn 1957; Gómez-Ramírez & Pound 1973; Dutta et al. 2001). More defects would be created if the fluid inclusion strained garnet due to fluid volume changes caused by changing *P*-*T* conditions. Although ilmenite needles are relatively common in garnet, multiphase needles rarely contain ilmenite. Consequently, it is likely that the ilmenite needles formed after the rutile needles. This is very strong evidence against a co-precipitation origin for garnet + oxide and multiphase needles.

The next step requires the elongated inclusions to equilibrate with the garnet structure by forming low-energy interfaces with garnet (Fig. 11c). This creates the hexagonal negative crystal shapes visible in cross-section. While the fluid is equilibrating with the garnet structure, the *P* and/or *T* environment of the rock as a whole would have been changing. Eventually it changed enough such that the internal overpressure within the inclusions exceeded that of the tensile strength of the garnet and the least compressive principal stress on the garnet causing decrepitation (Fig. 11d) (e.g., Stöckhert et al. 2001, 2009). Crystallization of the fluid would occur sometime after decrepitation due to further cooling and/or decompression, or due to the decrepitation event itself.

The negative crystal cross-section of the multiphase inclusions requires some delay between elongation and decrepitation. The inclusions would have to have decrepitated after elongating along <111> in order to preserve the radiating cracks, the negative crystal inclusion cross-sections, and the elongate shape. Our mechanism differs from previous explanations for elongated melt inclusions (e.g., Ferrero et al. 2012), as processes that crystallographically control melt movement within garnet are required.

Other Hypotheses:

Hypothesis 2: Precipitation (exsolution)

As rutile and ilmenite needles preferentially exsolve from garnet along <111>, it could be possible for other phases to precipitate out along with the oxides. For example, the Si and Mg needed to form quartz and phlogopite could have been derived from a majorite component in garnet, implying garnet core formation >5 GPa (e.g., Collerson et al. 2010). Garnet Na contents are elevated at HP/UHP conditions (e.g., Ono 1998; Hermann and Spandler 2008; Konzett and Frost 2009; Auzanneau et al. 2010); Na in the CT garnets could have gone into white mica and Phase-CV (Fig. 9a, Tables 2, 4). Ultrahigh pressures are necessary for K incorporation into garnet (e.g., Ono 1998; Wang and Takahashi 1999). However, the multiphase needles are thin so garnet would not necessarily need to contain large amounts of K to make the observed quantities of micas. It may also be possible that K and other elements were mobile and diffused into garnet to growing needles (e.g., Proyer et al. 2013). Garnets in UHP rocks have variable H_2O contents that can exceed 1000 ppm (e.g., Zheng 2009); this could have been a source for water in micas and Phase-CV. The exsolved water may have reacted with other phases in the inclusions to produce fluids/melts unlike those expected for partial melting of felsic rocks, perhaps accounting for the highly-siliceous Phase-CV compositions. Ni is elevated in garnet at mantle conditions and

528 can be used in thermometry (e.g., Canil 1999). The loss of Ni from garnet during needle
529 exsolution could explain the highly unusual Ni-rich phlogopite compositions (Table 3).
530 However, a severe problem with this hypothesis is that, as far as we are aware, the
531 exsolution of K-rich phases from garnet has never been documented from any geological setting.
532 K-feldspar, phlogopite, and phengite exsolution has been well studied in UHP clinopyroxene
533 (e.g., Shatsky et al. 1995; Katyama et al. 2002; Bozhilov et al. 2009; Dobrzhinetskaya et al.
534 2009; Sakamaki and Ogasawara 2014), but exsolution of such phases from garnet remains highly
535 speculative. In addition, there is no unequivocal evidence of UHP metamorphism for the CT
536 rocks.
537 **Hypothesis 3: Melting of pre-existing inclusions**
538 A third possibility is that polyphase mineral inclusions trapped during garnet growth
539 melted during heating (e.g., Perchuk et al. 2005, 2009) and then re-equilibrated with the host
540 garnet structure to form acicular inclusions. While this is a possibility, it seems unlikely. First, it
541 is unusual for melted polyphase inclusions to take on the negative crystal shape of their host
542 (Sobolev and Shimizu 1993; Perchuk et al. 2009). Second, the rather uniform size and phase
543 assemblage of the multiphase needles observed in garnets from multiple localities suggests that
544 they were not the product of melting of trapped mineral inclusions. If that were the case, the
545 needles would be expected to be more heterogeneous in composition, volume, and regional
546 distribution.
547 **Hypothesis 4: Infiltration including dissolution-precipitation**
548 Infiltration requires fluid entry into garnet followed by its crystallization along <111> of
549 garnet (e.g., Hwang et al. 2007). We consider this to be improbable because if fluid were to
550 infiltrate a garnet it would most likely flow in through fractures and other imperfections and

would not become crystallographically oriented. The slow diffusion of P provides additional evidence in this regard. The P map of needle-bearing garnet, while preserving detailed growth textures, shows no evidence of infiltration such as healed fractures communicating with the matrix (Fig. 9c).

Dissolution-precipitation of garnet also involves the entry of fluids. The garnet would be dissolved at an advancing dissolution front, and new garnet with a somewhat different composition would precipitate out behind (e.g. Putnis and John 2010). This process can in some cases produce oriented precipitates (e.g. Harlov et al. 2005). However, the preservation of original growth zoning in phosphorous, including overprint zonation, is inconsistent with this mechanism (Fig. 9c).

Implications

A growing number of localities recognized worldwide host garnets containing significant quantities of petrographically-obvious oriented Ti±Fe oxide needles (Fig. 12). With few exceptions, these rocks have undergone high- or ultrahigh-pressures, or very high temperatures near or above the UHT boundary of 900 °C. These *P* and/or *T* conditions are required to incorporate enough Ti into the garnet to produce Ti±Fe oxide needles during retrogression. A handful of localities contain both rutile and ilmenite needles, including the rocks described here (Fig. 12). As Ti diffusion in garnet is sluggish even at high-*T* (e.g. Hanger et al. 2014), the presence of rutile lamellae in comparatively low-*T* (~600–700 °C) garnet may indicate the involvement of additional formation mechanisms such as recrystallization. These would not, however, necessitate external Ti input to garnet. Only two examples of oriented mica-bearing multiphase needles containing or coexisting with oxide needles in garnet are known: the diamondiferous UHP Erzgebirge saidenbachite and the rocks of this study. However, it is

574 important to reiterate that we have not found any unequivocal UHP indicators such as coesite or
575 diamond in our rocks.

576 We conclude that the acicular, oriented multiphase inclusions originated as trapped fluid
577 inclusions that elongated during Ti±Fe oxide needle exsolution from garnet and subsequently
578 decrepitated during retrogression. Both the matrix ternary feldspar compositions and the high-Zr
579 contents of exsolved rutile needles in garnet from the upper member of the Bigelow Brook
580 Formation demonstrate that the rocks underwent UHT metamorphism ~1000 °C. This finding
581 extends the first described UHT locality in the United States (Brimfield Schist) to include a
582 second rock unit. Ongoing work indicates that UHTM occurred farther north in Massachusetts as
583 well (Ostwald et al. 2014). The cause of the high heat input into this area is yet to be determined
584 and will be the subject of future studies. As the only other documented locality containing
585 similar micaceous inclusions, the Erzgebirge of Germany, has also experienced *T* in excess of
586 1000 °C (and ultrahigh pressures), oriented acicular multiphase inclusions are likely to be useful
587 indicators of extreme temperatures and/or pressures.

588 **Acknowledgements**

589 We thank Xu Chu, Meng Tian, M.R. Ackerson, E. F. Baxter, N. C. Sullivan, and R. P.
590 Wintsch for discussions, J. O. Eckert, Jr. for microprobe analysis support, Z. Jiang for assistance
591 with EBSD measurements, Stewart's Gem Shop in Boise, Idaho for donation of Idaho star garnet
592 samples to the Yale Peabody Museum of Natural History, and two anonymous referees for their
593 reviews. Becker Construction Company kindly granted access to key exposures. Support from
594 the National Science Foundation Directorate of Geosciences (EAR-0744154, EAR-0948092, and
595 EAR-1250269) is gratefully acknowledged.

596

References Cited

Ackerson, M.R., Tailby, N., Watson, E.B. and Spear, F.S. (2013) Variations in Ti coordination and concentration in garnet in response to temperature, pressure and composition. Abstract. 2013 Fall Meeting, San Francisco, California.

Ague, J. (1995) Deep-crustal growth of quartz, kyanite and garnet into large-aperture, fluid-filled fractures, north-eastern Connecticut, USA. Journal of Metamorphic Geology, 13, 299-314.

Ague, J.J. and Carlson, W.D. (2013) Metamorphism as garnet sees it: The kinetics of nucleation and growth, equilibration, and diffusional relaxation. Elements, 9, 439-445.

Ague, J.J. and Eckert, J.O., Jr. (2012) Precipitation of rutile and ilmenite needles in garnet: Implications for extreme metamorphic conditions in the Acadian orogen, USA. American Mineralogist, 97, 840-855.

Ague, J.J., Eckert, J.O., Jr., Chu, X., Baxter, E.F. and Chamberlain, C.P. (2013) Discovery of ultrahigh-temperature metamorphism in the Acadian orogen, Connecticut, USA. Geology, 41, 271-274.

Alifirova, T.A., Pokhilenko, L.N., Ovchinnikov, Y.I., Donnelly, C.L., Riches, A.J., and Taylor, L.A. (2012) Petrologic origin of exsolution textures in mantle minerals: evidence in pyroxenitic xenoliths from Yakutia kimberlites. International Geology Review, 54, 1071-1092.

Armstrong, T.R., Tracy, R.J., and Hames, W.E. (1992) Contrasting styles of Taconian, eastern Acadian, and western Acadian metamorphism, central and western New England. Journal of Metamorphic Geology, 10, 415–426.

Auzanneau, E., Schmidt, M.W., Vielzeuf, D. and Connolly, J.A.D. (2010) Titanium in phengite: a geobarometer for high temperature eclogites. Contributions to Mineralogy and Petrology, 159, 1-24.

Benisek, A., Kroll, H. and Cemič, L. (2004) New developments in two-feldspar thermometry. American Mineralogist, 89, 1496-1504.

Benisek, A., Dachs, E. and Kroll, H. (2010) A ternary feldspar-mixing model based on calorimetric data: Development and application. Contributions to Mineralogy and Petrology, 160, 327-337.

Bozhilov, K.N., Xu, Z., Dobrzhinetskaya, L.F., Jin, Z. and Green, H.W. II (2009) Cation-deficient phlogopitic mica exsolution in diopside from garnet peridotite in SuLu, China. Lithos, 109, 304-313.

Brueckner , H.K. and Medaris, L.G. (2000) A general model for the intrusion and evolution of 'mantle' garnet peridotites in high-pressure and ultra-high-pressure metamorphic terranes. Journal of Metamorphic Geology, 18, 123-133.

Caby, R., Bruguier, O., Fernandez, L., Hammor, D., Bosch, D., Mechati, M., Laouar, R., Ouabadi, A., Abdallah, N., and Douchet, C. (2014). Metamorphic diamonds in a garnet

megacryst from the Edough massif (northeastern Algeria). Recognition and geodynamic consequences. Tectonophysics, 637, 341-353.

Cahn, J.W. (1957). Nucleation on dislocations. Acta Metallurgica, 5, 169-172.

Canil, D. (1999) The Ni-in-garnet geothermometer: Calibration at natural abundances. Contributions to Mineralogy and Petrology, 136, 240-246.

Carstens, H. (1971) Plastic stress relaxation around solid inclusions in pyrope. Contributions to Mineralogy and Petrology, 32, 289-294.

Carswell, D. and Van Roermund, H. (2005) On multi-phase mineral inclusions associated with microdiamond formation in mantle-derived peridotite lens at Bardane on Fjortoft, west Norway. European Journal of Mineralogy, 17, 31-42.

Cesare, B., Ferrero, S., Salvioli-Mariani, E., Pedron, D. and Cavallo, A. (2009) “Nanogranite” and glassy inclusions: The anatectic melt in migmatites and granulites. Geology, 37, 627-630.

Chamberlain, C.P. and Lyons, J.B. (1983) Pressure, temperature and metamorphic zonation Studies of pelitic schists in the Merrimack Synclinorium, South-Central New-Hampshire. American Mineralogist, 68, 530-540.

Clarke, G.L., Daczko, N.R. and Miescher, D. (2013) Identifying relic igneous garnet and clinopyroxene in eclogite and granulite, Breaksea orthogneiss, New Zealand. Journal of Petrology, 54, 1921-1938.

Collerson, K.D., Williams, Q., Kamber, B.S., Omori, S., Arai, H. and Ohtani, E. (2010) Majoritic garnet: A new approach to pressure estimation of shock events in meteorites and the encapsulation of sub-lithospheric inclusions in diamond. Geochimica et Cosmochimica Acta, 74, 5939-5957.

Dludla, S., le Roex, A.P. and Gurney, J.J. (2006) Eclogite xenoliths from the Premier kimberlite, South Africa: Geochemical evidence for a subduction origin. South African Journal of Geology, 109, 353-368.

Dobrzhinetskaya, L.F., Wirth, R., Rhede, D., Liu, Z. and Green, H.W. (2009) Phlogopite and quartz lamellae in diamond-bearing diopside from marbles of the Kokchetav massif, Kazakhstan: Exsolution or replacement reaction? Journal of Metamorphic Geology, 27, 607-620.

Donovan, J.J. and Tingle, T.N. (1996) An improved mean atomic number background correction for quantitative microanalysis. Microscopy and Microanalysis, 2, 1-7.

Dutta, B., Palmiere, E.J., & Sellars, C.M. (2001). Modelling the kinetics of strain induced precipitation in Nb microalloyed steels. Acta Materialia, 49, 785-794.

Emmanuel, S., & Ague, J.J. (2009). Modeling the impact of nano-pores on mineralization in sedimentary rocks. Water Resources Research, 45, W04406 .

Emmanuel, S., Ague, J.J., and Walderhaug, O. (2010). Interfacial energy effects and the evolution of pore size distributions during quartz precipitation in sandstone. Geochimica et Cosmochimica Acta, 74, 3539-3552.

Ewing, T.A., Hermann, J. and Rubatto, D. (2013) The robustness of the Zr-in-rutile and Ti-in-zircon thermometers during high-temperature metamorphism (Ivrea-Verbano Zone, northern Italy). Contributions to Mineralogy and Petrology, 165, 757-779.

Fahey, R. and Pease Jr, M. (1977) Preliminary bedrock geologic map of the South Coventry quadrangle. Tolland County, Connecticut: US Geological Survey Open-File Report, 77-587.

Ferrando, S., Frezzotti, M.L., Dallai, L. and Compagnoni, R. (2005) Multiphase solid inclusions in UHP rocks (Su-Lu, China): Remnants of supercritical silicate-rich aqueous fluids released during continental subduction. Chemical Geology, 223, 68-81.

Ferrero, S., Bartoli, O., Cesare, B., Salvioli-Mariani, E., Acosta-Vigil, A., Cavallo, A., Groppo, C. and Battiston, S. (2012) Microstructures of melt inclusions in anatectic metasedimentary rocks. Journal of Metamorphic Geology, 30, 303-322.

Frezzotti, M.L., Ferrando, S., Dallai, L. and Compagnoni, R. (2007) Intermediate alkali–alumino-silicate aqueous solutions released by deeply subducted continental crust: Fluid evolution in UHP OH-rich topaz–kyanite quartzites from Donghai (Sulu, China). Journal of Petrology, 48, 1219-1241.

Gomez-Ramirez, R., & Pound, G.M. (1973) Nucleation of a second solid phase along dislocations. Metallurgical Transactions, 4, 1563-1570.

Griffin, W.L., Jensen, B.B., and Misra, S.N. (1971) Anomalously elongated rutile in eclogite-facies pyroxene and garnet. Norsk Geologisk Tidsskrift, 51, 177–185.

694 Guinel, M.J.F. and Norton, M.G. (2006) The origin of asterism in almandine-pyrope garnets
695 from Idaho. Journal of Materials Science, 41, 719-725.

696 Hacker, B., Luffi, P., Lutkov, V., Minaev, V., Ratschbacher, L., Plank, T., Ducea, M., Patino-
697 Douce, A., McWilliams, M. and Metcalf, J. (2005) Near-ultrahigh pressure processing of
698 continental crust: Miocene crustal xenoliths from the Pamir. Journal of Petrology, 46,
699 1661-1687.

700 Haggerty, S.E. (1991) Oxide textures; a mini-atlas. Reviews in Mineralogy and Geochemistry,
701 25, 129-219.

702 Hanger, B. J., Yaxley, G.M., Jollands, M.C., and Hermann, J. (2014) Diffusion of major and
703 minor elements within zoned garnet from the Kaapvaal craton, as determined using
704 NanoSIMS and EPMA. In: *Goldschmidt Conference*, Sacramento, California.

705 Harlov, D.E., Wirth, R., and Forster, H.-J. (2005) An experimental study of dissolution–
706 reprecipitation in fluorapatite: fluid infiltration and the formation of monazite.
707 Contributions to Mineralogy and Petrology, 150, 268-286.

708 Hermann, J. and Rubatto, D. (2014) Subduction of continental crust to mantle depth:
709 Geochemistry of ultrahigh-pressure rocks. Treatise on Geochemistry 2nd Ed., p. 309-340.
710 Elsevier Science

711 Hermann, J. and Spandler, C.J. (2008) Sediment melts at sub-arc depths: An experimental study.
712 Journal of Petrology, 49, 717-740.

Hermann, J., Zheng, Y., and Rubatto, D. (2013) Deep fluids in subducted continental crust. Elements, 9, 281-287.

Hwang, S.L., Shen, P., Chu, H.T. and Yui, T.F. (2000) Nanometer-size a-PbO_2-type TiO_2 in garnet: A thermobarometer for ultrahigh-pressure metamorphism. Science, 288, 321-324.

Hwang, S.L., Yui, T.F., Chu, H.T., Shen, P., Schertl, H.P., Zhang, R.Y. and Liou, J.G. (2007) On the origin of oriented rutile needles in garnet from UHP eclogites. Journal of Metamorphic Geology, 25, 349-362.

Hwang, S.L., Shen, P., Chu, H.T., Yui, T.F., & Iizuka, Y. (2014). Origin of rutile needles in star garnet and implications for interpretation of inclusion textures in ultrahigh-pressure metamorphic rocks. Journal of Metamorphic Geology., in press, DOI: 10.1111/jmg.12119

Jiao, S., Guo, J., Mao, Q. and Zhao, R. (2011) Application of Zr-in-rutile thermometry: A case study from ultrahigh-temperature granulites of the Khondalite belt, North China Craton. Contributions to Mineralogy and Petrology, 162, 379-393.

Katayama, I., Ohta, M. and Ogasawara, Y. (2002) Mineral inclusions in zircon from diamond-bearing marble in the Kokchetav Massif, northern Kazakhstan. European Journal of Mineralogy, 14, 1103-1108.

Kawasaki, T. and Motoyoshi, Y. (2007) Solubility of TiO_2 in garnet and orthopyroxene: Ti thermometer for ultrahigh-temperature granulites. U.S. Geological Survey and The

National Academies; USGS OF-2007-1047, Short Research Paper 038; DOI: 10.3133/of2007-1047.srp038.

Kelsey, D.E. and Hand, M. (2014) On ultrahigh temperature crustal metamorphism: Phase equilibria, trace element thermometry, bulk composition, heat sources, timescales and tectonic settings. Geoscience Frontiers, in press, DOI: 10.1016/j.gsf.2014.09.006.

Keshav, S. and Sen, G. (2001) Majoritic garnets in Hawaiian xenoliths: preliminary results. Geophysical Research Letters, 28, 3509-3512.

Keshav, S., Sen, G. and Presnall, D.C. (2007) Garnet-bearing xenoliths from Salt Lake Crater, Oahu, Hawaii: High-pressure fractional crystallization in the oceanic mantle. Journal of Petrology, 48, 1681-1724.

Khomenko, V.M., Langer, K., Beran, A., Koch-Müller, M., and Fehr, T. (1994) Titanium substitution and OH-Bearing defects in hydrothermally grown pyrope crystals. Physics and Chemistry of Minerals, 20, 483–488.

Kohn, M.J. (2014) 4.7 - Geochemical Zoning in Metamorphic Minerals. In H.D. Holland and K.K. Turekian, Eds., Treatise on Geochemistry (Second Edition), p. 249-280. Elsevier, Oxford

Konzett, J, and Frost, D.J. (2009) The high *P*-*T* stability of hydroxyl-apatite in natural and simplified MORB—an experimental study to 15 GPa with implications for transport and storage of phosphorus and halogens in subduction zones. Journal of Petrology, 50, 2043-2062.

752 Kotkova, J., O'Brien, P.J. and Ziemann, M.A. (2011) Diamond and coesite discovered in
753 Saxony-type granulite: Solution to the Variscan garnet peridotite enigma. Geology, 39,
754 667-670.

755 Kroner, A., O'Brien, P.J., Nemchin, A.A. and Pidgeon, R.T. (2000) Zircon ages for high pressure
756 granulites from South Bohemia, Czech Republic, and their connection to Carboniferous
757 high temperature processes. Contributions to Mineralogy and Petrology, 138, 127-142.

758 Larsen, R.B., Eide, E.A. and Burke, E.A.J. (1998) Evolution of metamorphic volatiles during
759 exhumation of microdiamond-bearing granulites in the Western Gneiss Region, Norway.
760 Contributions to Mineralogy and Petrology, 133, 106-121.

761 Liu, S., Li, J. and Santosh, M. (2010) First application of the revised Ti-in-zircon
762 geothermometer to Paleoproterozoic ultrahigh-temperature granulites of Tuguiwula,
763 Inner Mongolia, North China Craton. Contributions to Mineralogy and Petrology, 159,
764 225-235.

765 Liu, Y., Gu, X., Li, S., Hou, Z. and Song, B. (2011a) Multistage metamorphic events in
766 granulitized eclogites from the North Dabie complex zone, central China: Evidence from
767 zircon U–Pb age, trace element and mineral inclusion. Lithos, 122, 107-121.

768 Liu, Y., Gu, X., Rolfo, F. and Chen, Z. (2011b) Ultrahigh-pressure metamorphism and
769 multistage exhumation of eclogite of the Luotian dome, North Dabie Complex Zone
770 (central China): Evidence from mineral inclusions and decompression textures. Journal of
771 Asian Earth Sciences, 42, 607-617.

772 Luvizotto, G. and Zack, T. (2009) Nb and Zr behavior in rutile during high-grade metamorphism
773 and retrogression: An example from the Ivrea–Verbano Zone. Chemical Geology, 261,
774 303-317.

775 Malaspina, N., Hermann, J., Scambelluri, M. and Compagnoni, R. (2006) Polyphase inclusions
776 in garnet–orthopyroxenite (Dabie Shan, China) as monitors for metasomatism and fluid-
777 related trace element transfer in subduction zone peridotite. Earth and Planetary Science
778 Letters, 249, 173-187.

779 Malitesta, C., Losito, I., Scordari, F. and Schingaro, E. (1995) XPS investigation of titanium in
780 melanites from Monte Vulture (Italy). European Journal of Mineralogy, 7, 847-858.

781 Manning, C.E. (2004). The chemistry of subduction-zone fluids. Earth and Planetary Science
782 Letters, 223, 1-16.

783 Manning, C.E. (2013) Thermodynamic modeling of fluid-rock interaction at mid-crustal to
784 upper-mantle conditions. Reviews in Mineralogy & Geochemistry, 76, 135-164.

785 Marschall, H.R., Kalt, A. and Hanel, M. (2003) *P-T* evolution of a Variscan lower-crustal
786 segment: A study of granulites from the Schwarzwald, Germany. Journal of Petrology,
787 44, 227-253.

788 Maruyama, S. and Parkinson, C.D. (2000) Overview of the geology, petrology and tectonic
789 framework of the high-pressure-ultrahigh-pressure metamorphic belt of the Kokchetav
790 Massif, Kazakhstan. Island Arc, 9, 439-455.

Massonne, H.-J. (2003) A comparison of the evolution of diamondiferous quartz-rich rocks from the Saxonian Erzgebirge and the Kokchetav Massif: Are so-called diamondiferous gneisses magmatic rocks? Earth and Planetary Science Letters, 216, 347-364.

Massonne, H.-J. and Brandelik, A. (1998) Ti in Al-garnet—a newly calibrated geothermobarometer for HP and UHP metamorphic rocks. Eos, 79, F972.

Mohammad, Y.O., Cornell, D.H., Danielsson, E., Hegardt, E.A., & Anczkiewicz, R. (2011). Mg-rich staurolite and kyanite inclusions in metabasic garnet amphibolite from the Swedish Eastern Segment: evidence for a Mesoproterozoic subduction event. European Journal of Mineralogy, 23, 609-631.

Mposkos, E.D. and Kostopoulos, D.K. (2001) Diamond, former coesite and supersilicic garnet in metasedimentary rocks from the Greek Rhodope: A new ultrahigh-pressure metamorphic province established. Earth and Planetary Science Letters, 192, 497-506.

Mposkos, E., Perraki, M. and Palikari, S. (2009) Single and multiphase inclusions in metapelitic garnets of the Rhodope Metamorphic Province, NE Greece. Spectrochimica Acta Part A-Molecular and Biomolecular Spectroscopy, 73, 477-483.

Obata, M. (1994) Material transfer and local equilibria in a zoned kelyphite from a garnet pyroxenite, Ronda, Spain. Journal of Petrology, 35, 271-287.

O'Brien, P.J. and Rotzler, J. (2003) High-pressure granulites: Formation, recovery of peak conditions and implications for tectonics. Journal of Metamorphic Geology, 21, 3-20.

O'Brien, P.J., Kroner, A., Jaeckel, P., Hegner, E., Zelazniewicz, A. and Kryza, R. (1997) Petrological and isotopic studies on palaeozoic high-pressure granulites, Gory Sowie Mts, Polish Sudetes. Journal of Petrology, 38, 433-456.

Ono, S. (1998) Stability limits of hydrous minerals in sediment and mid-ocean ridge basalt compositions: Implications for water transport in subduction zones. Journal of Geophysical Research, 103, 18,253-18,267.

Osanai, Y., Nakano, N., Owada, M., Nam, T.N., Miyamoto, T., Minh, N.T., Van Nam, N. and Van Tri, T. (2008) Collision zone metamorphism in Vietnam and adjacent South-eastern Asia: Proposition for Trans Vietnam Orogenic Belt. Journal of Mineralogical and Petrological Sciences, 103, 226-241.

Ostwald, C.E., Sullivan, N.C., Baxter, E.F., Ague, J.J. and Eckert, J.O., Jr. (2014) Discovery of a Neo-Acadian ultrahigh temperature metamorphic event in central Massachusetts via Sm-Nd garnet geochronology and Zr-in-rutile thermometry. Goldschmidt Conference, Sacramento, California, USA (in press).

Patel, S.C., Ravi, S., Thakur, S.S., Rao, T.K. and Subbarao, K.V. (2006) Eclogite xenoliths from Wajrakarur kimberlites, southern India. Mineralogy and Petrology, 88, 363-380.

Peper, J.D. and Pease, M.H. Jr. (1975) Geologic map of the Westford quadrangle, Connecticut. U.S. Geological Survey Quadrangle Map, GQ-1214.

Perchuk, A.L. (2008) Unusual inclusions in garnet from the diamond-bearing gneiss of the Erzgebirge, Germany. Geochemistry International, 46, 296-303.

Perchuk, A.L., Burchard, M., Maresch, W.V. and Schertl, H. (2005) Fluid-mediated modification of garnet interiors under ultrahigh-pressure conditions. Terra Nova, 17, 545-553.

Perchuk, A.L., Davydova, V.V., Burchard, M., Maresch, W.V., Schertl, H.-., Yapaskurt, V.O. and Safonov, O.G. (2009) Modification of mineral inclusions in garnet under high-pressure conditions: Experimental simulation and application to the carbonate-silicate rocks of Kokchetav massif. Russian Geology and Geophysics, 50, 1153-1168.

Proyer, A., Habler, G., Abart, R., Wirth, R., Krenn, K. and Hoinkes, G. (2013) TiO_2 exsolution from garnet by open-system precipitation: Evidence from crystallographic and shape preferred orientation of rutile inclusions. Contributions to Mineralogy and Petrology, 166, 211-234.

Putnis, A. and John, T. (2010) Replacement processes in the Earth's crust. Elements 6, 159-164.

Putnis, A., Prieto, M. and Fernandez-Diaz, L. (1995) Fluid supersaturation and crystallization in porous media. Geological Magazine, 132, 1–13.

Robinson, P. and Tucker, R.D. (1982) The Merrimack synclinorium in northeastern Connecticut. American Journal of Science, 282, 1735–1744.

Robinson, P., Tucker, R.D., Bradley, D., Berry, H.N. IV and Osberg, P.H. (1998) Paleozoic orogens in New England, USA. GFF, 120, 119-148.

Rodgers, J. (1981) The Merrimack synclinorium in northeastern Connecticut. American Journal of Science, 281, 176-186.

Rodgers (1985) Bedrock Geological Map of Connecticut, scale 1:125,000. Connecticut Geological and Natural History Survey, Department of Environmental Protection, Hartford, Connecticut.

Ruiz-Cruz, M.D. and Sanz de Galdeano, C. (2013) Coesite and diamond inclusions, exsolution microstructures and chemical patterns in ultrahigh pressure garnet from Ceuta (Northern Rif, Spain). Lithos, 177, 184-206.

Sajeev, K., Windley, B., Connolly, J. and Kon, Y. (2009) Retrogressed eclogite (20kbar, 1020 ºC) from the Neoproterozoic Palghat–Cauvery suture zone, southern India. Precambrian Research, 171, 23-36.

Sajeev, K., Kawai, T., Omori, S., Windley, B.F. and Maruyama, S. (2010) P-T evolution of Glenelg eclogites, NW Scotland: Did they experience ultrahigh-pressure metamorphism? Lithos, 114, 473-489.

Sakamaki, K. and Ogasawara, Y. (2014) Hydroxyl in clinopyroxene and titanite in a UHP diamond-free garnet-clinopyroxene rock from the Kokchetav Massif, northern Kazakhstan. International Geology Review, 56, 133-149.

Schmetzer, K., Bernhardt, H.-J. and Kiefert, L. (2002) Star garnet and star garnet cat's-eyes from Ambatondrazaka, Madagascar. Journal of Gemmology, 28, 13-23.

Schumacher, J.C., Schumacher, R., and Robinson, P. (1989) Acadian metamorphism in central Massachusetts and southwestern New Hampshire: evidence for contrasting P-T

trajectories. In J.S. Daly, R.A. Cliff, and B.W.D. Yardley, Eds., Evolution of Metamorphic Belts, 34, p. 453–460. Geological Society Special Publication, London.

Shatsky, V.S., Sobolev, N.V. and Vavilov, M.A. (1995) Diamond-bearing metamorphic rocks of the Kokchetav Massif (Northern Kazakhstan). In: Coleman RG and Wang X (eds.) Ultrahigh Pressure Metamorphism, pp. 427–455. Cambridge: Cambridge University Press.

Shen, P.Y., Hwang, S.L., Chu, H.T., Yu, T.F., Pan, C.N. and Huang, W.L. (2005) On the transformation pathways of alpha-PbO_2-type TiO_2 at the twin boundary of rutile bicrystals and the origin of rutile bicrystals. European Journal of Mineralogy, 17, 543-552.

Snoeyenbos, D.R. and Koziol, A.M. (2008) Exsolution Phenomena of UHP Type in Garnets From Western New England, USA. EOS, American Geophysical Union, V31E-07.

Snoeyenbos, D.R., Williams, M.L. and Hanmer, S. (1995) Archean high-pressure metamorphism in the western Canadian shield. European Journal of Mineralogy, 7, 1251-1272.

Sobolev, A. and Shimizu, N. (1993) Ultra-depleted primary melt included in an olivine from the Mid-Atlantic Ridge. Nature, 363, 151-153.

Song, S.G., Zhang, L.F. and Niu, Y.L. (2004) Ultra-deep origin of garnet peridotite from the North Qaidam ultrahigh-pressure belt, Northern Tibetan Plateau, NW China. American Mineralogist, 89, 1330-1336.

Stöckhert, B., Duyster, J., Trepmann, C. and Massonne, H.-J. (2001) Microdiamond daughter crystals precipitated from supercritical COH + silicate fluids included in garnet, Erzgebirge, Germany. Geology, 29, 391.

Stöckhert, B., Trepmann, C.A. and Massonne, H.-J. (2009) Decrepitated UHP fluid inclusions: About diverse phase assemblages and extreme decompression rates (Erzgebirge, Germany). Journal of Metamorphic Geology, 27, 673-684.

Streckeisen, A. (1979) Classification and nomenclature of volcanic rocks, lamprophyres, carbonatites, and melilitic rocks: Recommendations and suggestions of the IUGS Subcommission on the Systematics of Igneous Rocks. Geology, 7, 331-335.

Thomson, J.A. (2001) A counterclockwise *P-T* path for anatectic pelites, south-central Massachusetts. Contributions to Mineralogy and Petrology, 141, 623-641.

Tomkins, H.S., Powell, R. and Ellis, D.J. (2007) The pressure dependence of the zirconium-in-rutile thermometer. Journal of Metamorphic Geology, 25, 703-713.

Touret, J.L.R. and Huizenga, J.M. (2012) Charnockite microstructures: From magmatic to metamorphic. Geoscience Frontiers, 3, 745-753.

van Roermund, H.L.M and Drury, M.R. (1998) Ultra-high pressure (P > 6 GPa) garnet peridotites in Western Norway: Exhumation of mantle rocks from > 185 km depth. Terra Nova, 10, 295-301.

van Roermund, H.L.M., Drury, M.R., Barnhoorn, A. and De Ronde, A. (2000) Non-silicate inclusions in garnet from an ultra-deep orogenic peridotite. Geological Journal, 35, 209-229.

van Roermund, H.L.M., Carswell, D.A., Drury, M.R. and Heijboer, T.C. (2002) Microdiamonds in a megacrystic garnet websterite pod from Bardane on the island of Fjørtoft, western Norway: Evidence for diamond formation in mantle rocks during deep continental subduction. Geology, 30, 959-962.

Vrana, S. (2008) Mineral inclusions in pyrope from garnet peridotites, Kolin area, central Czech Republic. Journal of Geosciences, 53, 17-30.

Wang, W. and Takahashi, E. (1999) Subsolidus and melting experiments of a K-rich basaltic composition to 27 GPa; Implication for the behavior of potassium in the mantle. 84, 357-361.

Wang, L.P., Essene, E.J. and Zhang, Y.X. (1999) Mineral inclusions in pyrope crystals from Garnet Ridge, Arizona, USA: Implications for processes in the upper mantle. Contributions to Mineralogy and Petrology, 135, 164-178.

Whitney, D. L. (1992). High-pressure metamorphism in the Western Cordillera of North America. Journal of Metamorphic Geology, 10, 71-85.

Wintsch, R.P., Sutter, J.F., Kunk, M.J., Aleinikoff, J.N., and Dorais, M.J. (1992) Contrasting P-T-t paths: Thermochronologic evidence for a late Paleozoic final assembly of the Avalon composite terrane in the New England Appalachians. Tectonics, 11, 672–689.

Wintsch, R.P., Aleinikoff, J.N., Walsh, G.J., Bothner, W.A., Hussey, A.M.,II and Fanining, C.M. (2007) Shrimp U-Pb evidence for a late Silurian age of metasedimentary rocks in the Merrimack and Putnam-Nashoba terranes, eastern New England. American Journal of Science, 307, 119-167.

Wintsch, R.P., Aleinikoff, J.N. and Walsh, G.J. (2009) Late Silurian deposition and late Devonian metamorphism of gander cover at the southern end of the central maine terrane: Evidence from shrimp analysis of detrital zircons. Geological Society of America Abstracts with Programs, 41(3), 98.

Ye, K., Cong, B.L. and Ye, D.I. (2000) The possible subduction of continental material to depths greater than 200 km. Nature, 407, 734-736.

Zhang, R.Y. and Liou, J.G. (1999) Exsolution lamellae in minerals from ultrahigh-pressure rocks. International Geology Review, 41, 981-993.

Zhang, R.Y. and Liou, J.G. (2003) Clinopyroxenite from the Sulu ultrahigh-pressure terrane, eastern China: Origin and evolution of garnet exsolution in clinopyroxene. American Mineralogist, 88, 1591-1600.

Zhang, R.Y., Zhai, S.M., Fei, Y.W. and Liou, J.G. (2003) Titanium solubility in coexisting garnet and clinopyroxene at very high pressure: The significance of exsolved rutile in garnet. Earth and Planetary Science Letters, 216, 591-601.

Zheng, Y. (2009) Fluid regime in continental subduction zones: Petrological insights from ultrahigh-pressure metamorphic rocks. Journal of the Geological Society, 166, 763-782.

945 **Figure Captions**

946 **Figure 1.** Photomicrographs of inclusions in garnet from the southern end of the Central Maine
947 Terrane in northeastern Connecticut. Specimen numbers in square brackets for this and all
948 following figures. (**a**) Oriented rutile needles in garnet in cross-polarized light with conoscopic
949 illumination [124A-6]. (**b**) Close up of part **a** in plane-polarized light with oriented rutile (Rt),
950 ilmenite (Ilm), and multiphase needles (M).

951 **Figure 2.** Orientation of garnet containing multiphase (M) and rutile (Rt) needles from EBSD
952 measurements [124A-1]. Note the alignment of needles with garnet <111> and the rough
953 outlines of the multiphase needles.

954 **Figure 3.** Simplified geologic map of part of the Central Maine Terrane in northeastern
955 Connecticut, after Rodgers (1981, 1985), modified from Ague et al. (2013). Major west-dipping
956 faults are labeled. Sample localities with multiphase needle-bearing garnets denoted by yellow
957 diamonds. Other sample localities discussed in this paper, Ague and Eckert (2012), and Ague et
958 al. (2013) denoted by filled circles. Sample number prefix JAQ omitted for clarity. Bold text
959 indicates a multiphase needle bearing sample.

960 **Figure 4.** Common textures in rocks from the Upper Member of the Bigelow Brook Formation
961 and the Brimfield Schist, Connecticut. (**a**) Photo of a megacryst pseudomorph of sillimanite after
962 kyanite [131A]. (**b**) Photomicrograph of sillimanite with inclusions of spinel (Spl) and ilmenite
963 (Ilm) in plane-polarized light [125A]. (**c**) Photomicrograph of a garnet core containing
964 multiphase inclusions [27-7]. (**d**) Photomicrograph of plagioclase antiperthite in cross-polarized
965 light [173A].

966 **Figure 5.** Illustrations of garnets showing example core-rim relationships and the locations of
967 inclusions. (**a**) A large garnet with a sharp core-rim boundary marked by the appearance of
968 sillimanite surrounding the core. The core contains an area of biotite inclusions surrounded by
969 rutile, ilmenite, and multiphase needles [124A-1]. (**b**) Garnet with a sharp core-rim boundary
970 roughly outlined by quartz inclusions [141B]. Rutile, ilmenite, and multiphase needles occur in
971 the central part of the garnet core.

972 **Figure 6.** Backscattered electron images of cross sections of multiphase needles in garnet from
973 sample 124A-6. Images (a) – (h) taken perpendicular to long axis of needles; images (i) and (j)
974 taken sub-parallel to long axes. Qtz=quartz, Phl=phlogopite, WM=white mica, Rt=rutile,
975 G=graphite, Phase-CV=siliceous compositionally variable phase. (**a**) Multiphase needle showing
976 negative garnet crystal shape and cracks radiating out from the corners. (**b**) Multiphase needle
977 containing phlogopite and quartz surrounding a rutile needle. (**c**) Multiphase needle with fine-
978 grained quartz and phlogopite surrounding a graphite rod. (**d**) Multiphase needle displaying
979 negative garnet crystal shape and radiating cracks. The inclusion contains finely intergrown
980 phlogopite, quartz, and white mica around rutile. (**e**) Multiphase needle containing a complex
981 intergrowth of phlogopite, quartz, and Phase-CV with two rutile needles. (**f**) Multiphase needle
982 with well-developed negative crystal shape of garnet. White mica, phlogopite, and quartz
983 interfinger with each other. (**g**) Multiphase needle that has negative crystal shape of garnet and
984 common granophyre-like quartz-mica intergrowths. (**h**) Multiphase needle roughly parallel to the
985 thin section surface. Rutile crystal lies parallel to the elongation direction of the needle. Quartz
986 and phlogopite are finely intergrown. (**i**) Multiphase needle roughly parallel to the thin section
987 surface. Rutile crystal lies parallel to the elongation direction of the needle. The inclusion
988 contains a complex intergrowth of phlogopite, white mica, and quartz.

Figure 7. Chemical maps of multiphase needles in garnet. Maps (a) and (b) made sub-parallel to long axis of needles; maps (c) and (d) made perpendicular to long axes. BSE=Backscattered electron image, Als=Al_2SiO_5 polymorph, Qtz=quartz, Phl=phlogopite, WM=white mica, Rt=rutile, G=graphite, Mnz=monazite, Zrn=zircon, Phase-CV=siliceous compositionally variable phase. (**a**) Multiphase needle containing phlogopite, quartz, rutile, and zircon [27-7]. (**b**) Multiphase needle shown previously in Figure 5g showing the complex intergrowth of quartz, micas, and rutile [124A-6]. (**c**) Multiphase needle containing monazite, rutile, and phlogopite with finely intergrown quartz and Phase-CV [141B]. (**d**) Multiphase needle composed of Phase-CV. Note the variable composition of Phase-CV. The high Al features in the map (red) are artifacts of the void at the southern end of the inclusion [172A].

Figure 8. Chemical zoning profiles from rim to core across a representative garnet [124A-6]. Exsolved oxides and multiphase needles are present in the shaded gray region. (**a**) Molar Mg/Fe. (**b**) Mn atoms per formula unit (a.f.u.). (**c**) Ca. (**d**) Ti. Note the Ti growth zoning in the rim and the drop in Ti concentration where exsolved rutile and ilmenite needles are located. (**e**) P. The abrupt drop in P in the core region is due to overprint zonation (see Fig. 7). (**f**) Y. Note the decrease in Y from core to rim.

Figure 9. Chemical zoning profiles from rim to core across a garnet along with a phosphorus map of the garnet of the same area [124A-2]. (**a**) Na atoms per formula unit (a.f.u.). (**b**) P. The abrupt drops in P are due to overprint zonation as shown in part (c). (**c**) Phosphorus map of garnet. Note the core rim-boundary marked by a sharp change in P content as well as the low-P patches within the garnet core due to overprint zonation. Line of traverse shown in part (b) is slightly irregular to avoid cracks, pits, and inclusions.

Figure 10. Ternary Quartz-Orthoclase-Anorthite+Albite diagram for CIPW norms of Phase-CV analyses in Table 4. The rock names are from the Quartz-Alkali feldspar-Plagioclase (QAP) diagram of the IUGS classification scheme (Streckeisen 1979). Strictly speaking, the QAP diagram should be based on modes whenever possible, but chemical (e.g., normative) mineralogical proxies can be used if the material is amorphous or too fine grained for modal analysis.

Figure 11. Illustration showing the steps of multiphase needle formation as proposed by the trapped fluid hypothesis (Hypothesis 1). (**a**) Ti-bearing garnet grows and entraps fluid. (**b**) Cooling and/or decompression cause rutile exsolution. Entrapped fluid can propagate through the garnet and elongate either by adhering to a growing rutile needle or moving due to internal overpressure within the fluid inclusion by following points of weakness in the garnet structure along <111>. As the multiphase needles rarely contain ilmenite, it is likely that the ilmenite exsolved at a later time. (**c**) Over time the inclusions texturally equilibrate with the garnet structure by developing low-energy interfaces shown by the hexagonal negative garnet crystal cross-sections of the inclusions. (**d**) Further cooling and/or decompression causes the internal overpressure within the inclusions to exceed the combination of the tensile strength of the garnet host and least principle compressive stress such that decrepitation occurs. Crystallization of fluid occurs during or after decrepitation.

Figure 12. Examples of published *P*-*T* estimates for rocks containing garnet with petrographically-obvious oriented Ti±Fe oxide needle inclusions modified from Ague and Eckert (2012). *T* at maximum *P* (if known) is plotted. Arrows indicate that *T* or *P* estimate is a minimum. Uncertainties shown if given in original publication. A: Edough Massif, northeastern

Algeria (Caby et al 2014). B: omphacite granulite, Breaksea Orthogneiss, New Zealand (Clarke et al. 2013). BM: diamondiferous felsic granulites, Bohemian Massif (Kröner et al. 2000; O'Brien and Rötzler 2003; Hwang et al. 2007; Kotkavá et al. 2011). BR: diamondiferous granulite of Cueta, Betic-Rif cordillera, Africa (Ruiz-Cruz and de Galdeano 2013). C: garnet peridotites, Kolín area, central Czech Republic (Vrána 2008). E: Saxonian Erzgebirge, Saidenbach reservoir (Hwang et al. 2000; Massonne 2003; Hermann and Rubatto 2014). G: Eclogite, Glenelg, NW Scotland (Sajeev et al. 2010). GR: Mantle garnet xenocrysts, Garnet Ridge, Arizona (Wang et al. 1999). Ha: Hawaiian xenoliths (Keshav and Sen 2001; Keshav et al. 2007). J: Eclogite, Junan, Sulu UHP terrane (Zhang et al. 2003). K: Kulet whiteschist, Kokchetav Massif (Maruyama and Parkinson 2000; Shen et al. 2005). L: Eclogite, Luotian dome, North Dabie Complex Zone, Central China (Malaspina et al. 2006; Liu et al. 2011a,b). M: Felsic granulites, Tuguiwula, Inner Mongolia, North China Craton (Liu et al. 2010).N: mafic granulite, Ngoc Linh Complex, Vietnam (Osanai et al. 2008). NQ: Garnet peridotite, North Qaidam, Tibetan Plateau (Song et al. 2004). O: Garnet peridotite, Otrøy, Western Gneiss Region, Norway (van Roermund et al. 2000). P: granulite xenolith, Pamir, India (Touret and Huizenga 2012; Hacker et al. 2005). PC: Eclogite, Palghat-Cauvery suture zone, India (Sajeev et al. 2009) PK: Eclogite xenoliths, Premier Kimberlite (Dludla et al. 2006). R: Garnet pyroxenite, Ronda, Spain (Obata 1994; Brueckner and Medaris 2000). Rh: Metapelitic rocks, Greek Rhodope (Mposkos and Kostopoulos 2001). Rz: Rizhao garnet clinopyroxenite, Sulu UHP terrane (Zhang and Liou 2003). S: Granulites from the Schwarzwald, Germany (Marschall et al. 2003). *P-T* estimate is a minimum. Sb: High-pressure granulite, Snowbird tectonic zone, Canada (Snoeyenbos et al. 1995). *P-T* estimate is a minimum. SM: Eclogite, Song Ma suture zone, Vietnam (Osanai et al. 2008). Sw : Borås Mafic Intrusion of the Swedish Eastern Segment (Mohammad et al. 2011). W:

Eclogite xenolith, Wajrakarur kimberlites, southern India (Patel et al. 2006). WGR: Felsic granulite, Western Gneiss Region, Norway (Larsen et al. 1998; Hermann and Rubatto 2014). Y: Yangkou ultramafic-mafic complex, Sulu UHP terrane (Zhang et al. 2003). Ya : Yakutia kimberlites, Siberian Craton (Carstens 1971; Alifirova et al. 2011). Garnets from the Skagit gneiss (not shown) in the North Cascades, Washington, USA and British Columbia, Canada also contain oriented rutile needles (Whitney 1992). The minimum *T* is 700–725 °C (at 0.8-1.0 GPa) based on petrogenetic grid considerations. However, most gneiss garnet-biotite *T* estimates are 800-1000 °C (Whitney 1992). These high *T* estimates were interpreted to be due to retrogression, but perhaps reflect actual peak conditions.

Table 1. Rutile analyses

	Needle Rt-2 124A-2	Needle Rt-3 124A-2	Needle Rt-4 124A-6	Needle Rt-7 124A-2	Needle Rt-8 124A-6	Needle Rt-9 124A-6	Needle Rt-10 124A-6	Needle Rt-12 124A-6	Needle Rt-17 124A-6	Needle Rt-18* 124A-6	Matrix Rt-1 124A-6	Matrix Rt-2 124A-6	Matrix Rt-3 124A-6	Matrix Rt-4 124A-6	Matrix Rt-5 124A-6
SiO_2	0.10	0.11	0.10	0.20	0.13	0.12	0.11	0.11	0.12	0.18	0.02	0.04	0.03	0.06	0.05
TiO_2	93.98	94.35	94.05	94.44	94.84	94.09	95.47	95.13	95.84	94.77	98.01	97.77	98.58	96.16	98.33
ZrO_2	0.920	1.078	1.037	0.914	0.986	1.043	1.174	1.167	1.225	1.308	0.098	0.054	0.068	0.093	0.077
Al_2O_3	0.06	0.06	0.04	0.12	0.08	0.10	0.06	0.13	0.05	0.09	0.02	0.05	0.05	0.07	0.06
Cr_2O_3	0.10	0.14	0.11	0.13	0.08	0.10	0.07	0.05	0.06	0.13	0.36	0.27	0.33	0.36	0.09
Nb_2O_5	0.78	0.77	0.88	1.13	0.79	1.19	0.36	0.45	0.28	0.42	0.12	0.45	0.48	0.88	0.37
Ta_2O_5	0.04	0.03	0.04	0.01	0.02	0.06	0.01	b.d.	0.03	0.03	b.d.	b.d.	0.03	0.13	0.02
V_2O_5	0.91	0.79	0.75	0.81	0.95	0.90	0.80	0.71	0.74	0.57	1.26	1.07	0.95	1.38	0.54
Fe_2O_3	1.81	1.93	2.18	2.11	2.26	2.08	1.79	2.24	1.99	1.90	0.05	0.17	0.20	0.20	0.27
MnO	0.01	0.04	0.01	0.03	0.03	0.03	0.04	0.02	0.04	0.06	0.04	b.d.	0.02	b.d.	b.d.
MgO	0.01	0.01	0.01	0.03	0.02	0.02	0.01	0.01	0.01	0.06	0.01	b.d.	b.d.	b.d.	b.d.
Total	98.73	99.30	99.22	99.93	100.17	99.73	99.90	99.84	100.39	99.41	99.99	99.87	100.74	99.33	99.81
							Structural Formulas (2 O)								
Si	0.001	0.002	0.001	0.003	0.002	0.002	0.002	0.001	0.002	0.002		0.001		0.001	0.001
Ti	0.961	0.960	0.958	0.955	0.956	0.954	0.964	0.960	0.964	0.963	0.981	0.980	0.980	0.971	0.986
Zr	0.006	0.007	0.007	0.006	0.006	0.007	0.008	0.008	0.008	0.008	0.001			0.001	0.001
Al	0.001	0.001	0.001	0.002	0.001	0.002	0.001	0.002	0.008	0.001		0.001	0.001	0.001	0.001
Cr	0.001	0.002	0.001	0.001	0.001	0.001	0.001	0.001	0.001	0.001	0.004	0.003	0.004	0.004	0.001
Nb	0.005	0.005	0.005	0.007	0.005	0.007	0.000	0.003	0.002	0.002	0.001	0.003	0.003	0.005	0.002
Ta														0.001	
V	0.008	0.007	0.007	0.007	0.008	0.008	0.007	0.006	0.007	0.007	0.011	0.010	0.008	0.012	0.005
Fe^{3+}	0.019	0.020	0.022	0.021	0.023	0.021	0.018	0.023	0.020	0.019	0.001	0.002	0.002	0.002	0.003
Mn									0.001	0.001					
Mg				0.001	0.001										
T (°C) at 1.0 GPa:	984	1008	1002	984	995	1003	1021	1020	1028	1038	*T* (°C) at 0.6 GPa:	700	654	673	700	684

Notes: b.d. = below detection, Rt = Rutile. All Fe as Fe^{3+}. V counts corrected for Ti interference; Cr counts corrected for V interference. The thermometer of Tomkins et al. (2007) was used for all temperature estimates. A pressure of 1.0 GPa corresponding to the minimum peak pressure from Ague et al. (2013) was used for temperature estimates for rutile needles. 0.6 GPa was used for matrix rutile assuming re-equilibration during exhumation (Ague et al. 2013). *Rutile within a multiphase needle coexisting with quartz (Fig. 5b).

Table 2. Garnet analyses

	124A-6 SE-Rim	124A-6 Core	165A-2 Near Rim	165A-2 Core	172A Near Rim	172A Core
SiO_2	37.74	37.69	38.48	38.23	38.43	38.14
TiO_2	0.013	0.006	0.029	0.024	0.040	0.018
P_2O_5	0.042	0.067	0.043	0.044	0.057	0.047
Al_2O_3	21.72	21.74	21.96	21.90	21.65	21.92
Cr_2O_3	0.04	0.02	0.02	0.01	0.02	0.01
Y_2O_3	0.01	0.08	b.d.	b.d.	b.d.	0.04
FeO	31.43	30.61	28.84	30.33	28.59	28.98
MgO	6.76	6.59	8.23	7.28	8.02	8.29
MnO	0.93	0.93	0.46	0.54	1.00	1.01
CaO	1.27	1.68	1.34	1.31	1.20	0.91
Na_2O	0.018	0.030	0.009	0.009	0.007	0.010
Total	99.97	99.45	99.41	99.56	99.01	99.38
			Structural Formulas (12 O)			
Si	2.961	2.971	2.999	2.993	3.013	2.977
Ti	0.0008	0.0004	0.0017	0.0014	0.0024	0.0011
P	0.0028	0.0045	0.0028	0.0029	0.0038	0.0031
^{IV}Al	0.039	0.029	0.001	0.007		0.023
^{VI}Al	1.969	1.990	2.016	2.013	2.000	1.993
Cr	0.003	0.001	0.001	0.001	0.001	0.001
Y		0.003				0.002
Fe^{2+}	2.003	1.993	1.905	2.002	1.882	1.874
Fe^{3+}	0.059	0.025			0.002	0.018
Mg	0.791	0.774	0.956	0.850	0.943	0.965
Mn	0.062	0.062	0.030	0.036	0.067	0.067
Ca	0.107	0.142	0.112	0.110	0.101	0.076
Na	0.0027	0.0046	0.001	0.0014	0.0011	0.0015

Notes: b.d. = below detection. Blank in wt. % table means element or oxide not analyzed. Fe^{2+} and Fe^{3+} in garnet estimated based on 8 cations per 12 O. By convention, garnet ^{IV}Al is amount needed to fill the tetrahedral sites; however, actual site occupancies have not been determined. Zr and K are b.d. and are not tabulated; detection limits: ~80 ppm (Zr) and ~20 ppm (K). Near Rim values exclude analyses directly at the garnet rims affected by retrograde drops in Mg/Fe and increases in Mn.

Table 3. Mica analyses

	Phl-1 124A-6	Phl-2 124A-6	Phl-3 124A-6	Phl/WM-1 124A-6	Phl/WM-2 124A-6	WM-1ab 124A-6	WM-2 124A-6
SiO_2	37.16	39.00	38.02	46.68	42.50	49.32	45.67
TiO_2	0.54	0.24	0.52	b.d.	0.41	0.08	0.03
Al_2O_3	18.19	20.24	17.53	30.79	23.43	32.32	34.38
Cr_2O_3	0.61	0.08	0.52	b.d.	0.61	0.03	0.03
FeO	9.02	8.95	7.53	3.32	5.83	2.61	1.87
MnO	1.08	b.d..	0.96	b.d..	0.88	0.19	0.12
NiO	2.66	b.d..	0.94	b.d..	2.40	0.14	b.d.
MgO	16.54	18.14	19.70	5.37	9.84	1.66	1.09
CaO	0.30	0.05	0.39	0.06	0.32	0.19	0.03
BaO	0.82	0.22	0.62	0.16	0.88	0.10	b.d.
Na_2O	0.44	0.33	0.84	1.78	1.28	3.44	1.60
K_2O	9.14	9.09	7.69	8.26	8.35	5.34	7.83
F	0.18	0.03	1.29	b.d..	0.22	0.14	b.d.
Cl	0.18	0.08	0.19	0.03	0.18	0.03	0.01
Total	96.74	96.42	96.16	96.44	97.00	95.52	92.66
			Structural Formulas (11 O)				
Si	2.722	2.767	2.751	3.099	2.973	3.228	3.100
^{IV}Al	1.278	1.233	1.250	0.901	1.027	0.772	0.900
∑IV	4.000	4.000	4.000	4.000	4.000	4.000	4.000
Ti	0.030	0.013	0.028		0.022	0.004	0.002
^{VI}Al	0.292	0.460	0.245	1.508	0.905	1.721	1.850
Cr	0.035	0.005	0.030		0.034	0..002	0.002
Fe	0.553	0.531	0.456	0.184	0.341	0.143	0.106
Mn	0.067		0.059		0.052	0.011	0.007
Ni	0.157		0.055		0.135	0.007	
Mg	1.806	1.919	2.125	0.532	1.027	0.162	0.110
∑VI	2.940	2.927	2.997	2.224	2.515	2.049	2.077
Ca	0.024	0.004	0.030	0.005	0.024	0.013	0.002
Ba	0.024	0.006	0.018	0.004	0.024	0.003	
Na	0.063	0.045	0.118	0.229	0.173	0.436	0.211
K	0.854	0.823	0.709	0.699	0.745	0.446	0.678
∑XII	0.965	0.878	0.875	0.937	0.967	0.898	0.891
F	0.043	0.006	0.296		0.049	0.029	
Cl	0.022	0.009	0.024	0.004	0.021	0.003	0.001
Mg/(Mg+Fe)	0.77	0.78	0.82	0.74	0.75	0.53	0.51

Notes: b.d. = below detection. Phl = Phlogopite, WM = White Mica, Phl/WM = finely intergrown phlogopite and white mica. By convention, ^{IV}Al mica is amount needed to fill the tetrahedral sites; however, actual site occupancies have not been determined. Oxygen equivalent of F^- and Cl^- subtracted from totals. Fe as Fe^{2+}.

Table 4. Phase-CV analyses

	MI-1 124A-6	MI-2 124A-6	MI-3 124A-6	MI-6 124A-6	MI-9 124A-6	MI-1 124A-2	MI-2 124A-2	M1-2a 141B	MI-2b 141B	MI-2c 141B	MI-1a 172A	MI-1b 172A
SiO_2	68.26	86.33	77.15	59.48	71.69	75.89	73.12	94.26	76.23	83.09	89.78	89.78
TiO_2	b.d.	0.06	b.d.	0.15	b.d.	0.06	b.d.	0.32	0.15	0.04	b.d.	b.d.
Al_2O_3	22.46	6.14	16.13	26.68	17.31	14.99	16.61	0.60	18.33	12.53	4.63	4.63
Cr_2O_3	b.d.	0.04	0.08	0.15	b.d.	b.d.	0.10	b.d.	0.04	0.04	0.20	0.20
FeO	2.79	2.72	2.22	1.53	1.94	1.42	1.55	1.35	1.61	1.17	1.10	1.10
MnO	b.d.	0.08	0.19	0.12	0.18	0.61	0.04	b.d.	0.15	b.d.	0.12	0.12
NiO	0.27	b.d.	0.74	0.13	b.d.	b.d.	b.d.	0.74	0.27	b.d.	0.27	0.27
MgO	4.33	2.30	1.77	0.97	2.10	0.07	1.32	0.19	0.37	0.05	0.03	0.03
CaO	b.d.	0.04	0.07	4.33	0.74	3.09	2.38	0.05	1.06	0.97	0.26	0.26
BaO	0.06	0.20	b.d.	b.d.	b.d.	0.13	0.14	b.d.	0.03	0.03	0.13	0.13
Na_2O	0.01	0.17	0.03	4.44	1.64	3.50	0.96	0.04	0.10	0.05	2.31	2.31
K_2O	0.01	1.99	0.05	0.68	1.89	0.51	0.15	0.06	0.08	0.02	0.04	0.04
F	b.d.	0.08	0.09	b.d.	b.d.	0.01	0.03	0.04	b.d.	0.01	b.d.	b.d.
Cl	0.02	0.05	b.d.	0.02	b.d.	0.01	b.d.	b.d.	b.d.	0.01	0.02	0.02
Total	98.20	100.18	98.49	98.68	97.39	100.28	96.39	97.62	98.42	98.00	98.87	97.70
						CIPW Norm (wt. %)						
Quartz	60.15	71.89	72.64	19.47	49.69	44.88	34.97	94.27	72.02	81.33	75.15	76.85
Anorthite				21.78	3.77	15.21	11.54		5.36	4.84	1.29	1.09
Albite		0.70	0.25	37.78	14.22	29.38	41.80	0.34	0.85	0.28	19.50	16.92
Orthoclase	0.28	12.49	0.30	4.08	11.46	3.49	1.39	0.35	0.58	0.23	0.71	1.65
Corundum	22.82	3.71	16.27	10.97	11.51	3.03	3.93	0.48	16.39	10.91	0.29	1.12
Hypersthene	16.68	10.72	10.21	5.36	9.34	3.82	6.08	3.81	4.43	2.21	2.64	2.04
Ilmenite		0.11	0.02	0.28		0.11		0.63	0.28	0.08		0.28
Chromite		0.06	0.12	0.22			0.15		0.06	0.06	0.29	0.03
Halite	0.04	0.09		0.04		0.02				0.02	0.04	
Fluorite		0.20	0.22			0.02	0.07	0.10		0.02		

Notes: b.d. = below detection. MI = Multiphase Inclusion. Fe as Fe^{2+}. Totals below 99 wt. % are assumed to be due to a hydrous component. Oxygen equivalent of F^- and Cl^- subtracted from totals.

Table 5. Spinel and ilmenite inclusions in sillimanite pseudomorph after kyanite, sample 125A

	Spl-1	Spl-2	Ilm-1	Ilm-2
SiO_2	0.03	0.03	0.04	0.04
TiO_2	b.d.	0.04	52.04	52.50
Al_2O_3	59.44	59.40	0.08	0.05
Cr_2O_3	0.41	0.30	0.01	0.06
Nb_2O_5	0.02	b.d.	0.13	0.14
Ta_2O_5	b.d.	0.02	0.01	0.02
V_2O_5	0.15	0.09	0.15	0.17
Fe_2O_3	0.79	1.21	1.32	0.81
FeO	22.49	24.05	44.89	44.16
ZnO	7.65	7.21	b.d.	0.01
MnO	0.04	0.05	0.25	0.25
NiO	b.d.	0.10	0.03	0.04
MgO	7.48	6.84	1.03	1.62
Total	98.50	99.33	99.97	99.79
	Structural Formulas			
	Spinel (4 O)		**Ilmenite (3 O)**	
Si	0.001	0.001	0.001	0.001
Ti		0.001	0.982	0.987
Al	1.968	1.962	0.002	0.002
Cr	0.009	0.007		0.001
Nb			0.002	0.001
Ta				
V	0.003	0.002	0.003	0.003
Fe^{2+}	0.528	0.564	0.941	0.923
Fe^{3+}	0.017	0.025	0.025	0.015
Zn	0.159	0.149		
Mn	0.001	0.001	0.005	0.005
Ni		0.002	0.004	0.001
Mg	0.313	0.286	0.039	0.060

Notes: b.d. = below detection. Spl = spinel, Ilm = ilmenite. FeO and Fe_2O_3 calculated using two cations per three O atoms for ilmenite and three cations per four O atoms for spinel. V counts corrected for Ti interference; Cr counts corrected for V interference.

Table 6. Feldspar (antiperthite) analyses

	Pl-1 Host 167A	Kfs-1 Exsolution 167A	Pl-2 Host 167A	Kfs-2 Exsolution 167A	Pl-6 Host 167A	Kfs-6 Exsolution 167A	Pl-1 Host 173A	Kfs-1 Exsolution 173A
SiO_2	59.82	64.66	59.82	64.60	60.31	64.65	57.95	64.27
Al_2O_3	25.05	18.95	25.13	18.98	25.29	18.89	26.92	18.85
FeO	0.03	0.01	0.03	0.02	0.03	0.03	0.03	0.02
MnO	0.02	0.01	0.01	0.02	0.01	0.02	0.01	b.d.
MgO	0.01	b.d.	b.d.	b.d.	0.01	b.d.	b.d.	b.d.
CaO	6.51	0.06	6.49	0.06	6.47	0.06	8.32	0.08
BaO	0.02	0.31	0.02	0.33	0.01	0.29	0.02	0.27
Na_2O	7.79	0.86	7.86	1.03	7.77	0.77	6.78	0.60
K_2O	0.24	15.39	0.22	15.07	0.26	15.39	0.26	15.68
Total	99.48	100.25	99.58	100.10	100.17	100.19	100.30	99.77
				Structural Formulas (8 O)				
Si	2.679	2.979	2.676	2.977	2.680	2.981	2.587	2.978
Al	1.322	1.029	1.325	1.031	1.325	1.027	1.417	1.029
Fe	0.001		0.001	0.001	0.001	0.001	0.001	0.001
Mn				0.001		0.001		
Mg					0.001			
Ca	0.312	0.003	0.311	0.003	0.308	0.003	0.398	0.004
Ba		0.006		0.006		0.005		0.005
Na	0.676	0.077	0.682	0.092	0.670	0.069	0.587	0.054
K	0.014	0.904	0.013	0.886	0.015	0.905	0.015	0.927
X_{An}	0.311	0.003	0.309	0.003	0.310	0.003	0.398	0.004
X_{Ab}	0.675	0.078	0.678	0.094	0.675	0.071	0.587	0.055
X_{Or}	0.014	0.919	0.013	0.903	0.015	0.926	0.015	0.941
Vol. %	77.1	22.9	80.9	19.1	78.6	21.4	84.3	15.7

	Reintegrated Compositions and Temperature Estimates			
X_{An}	24.6	25.5	24.9	34.1
X_{Ab}	54.7	57.5	55.4	50.9
X_{Or}	20.7	17.0	19.7	15.0
T (°C)	1005 *956*	973 *921*	998 *948*	983 *999*

Notes: b.d. = below detection. Pl= Plagioclase, Kfs = Potassium Feldspar, Vol. % = volume percent phase in antiperthite. All Fe as Fe^{2+}. Temperature estimates using the feldspar activity model of Benisek et al. (2004) are shown in plain text and temperature estimates italicized were done using the feldspar activity model of Benisek et al. (2010).

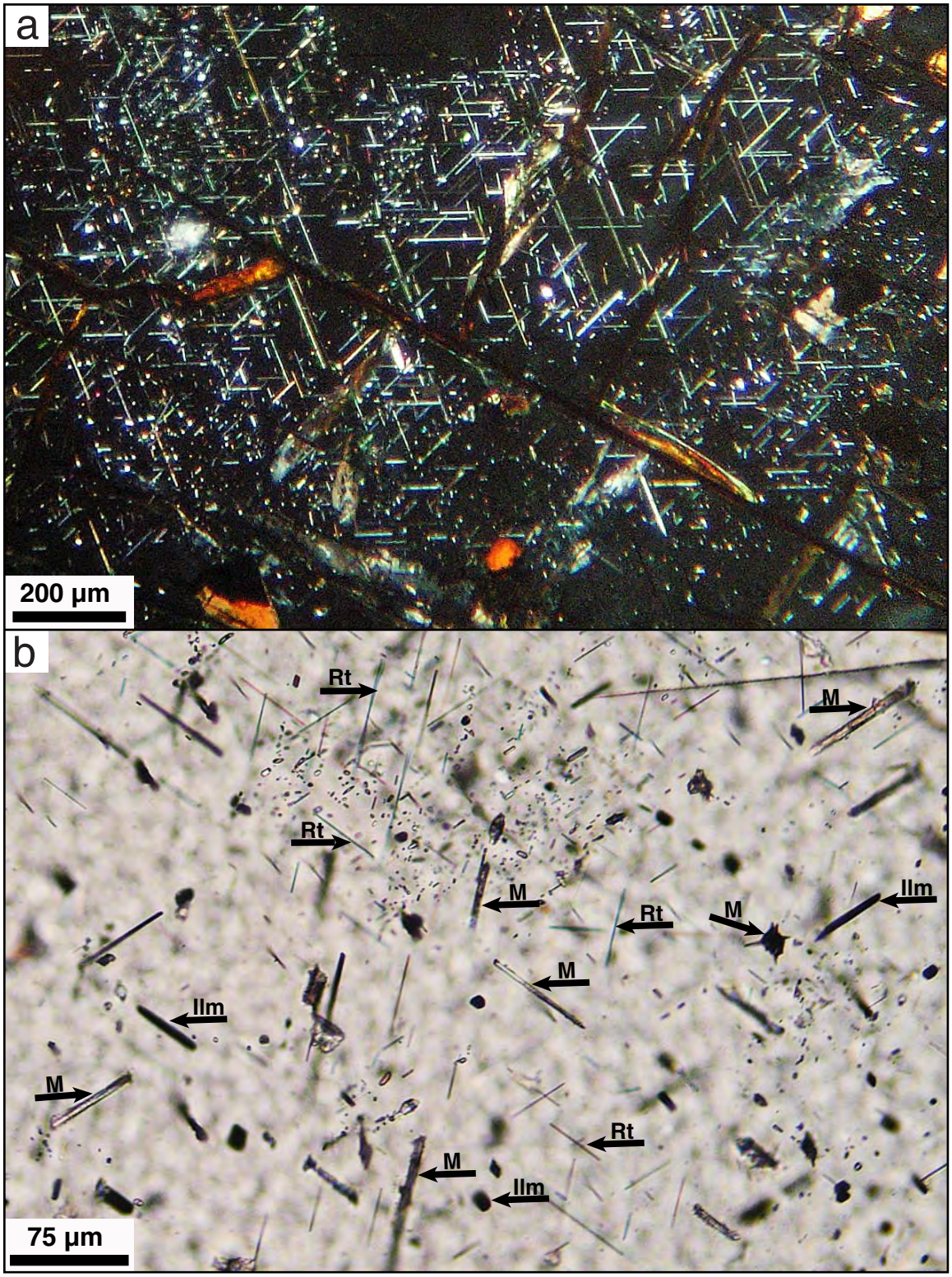

Figure 1. Axler and Ague

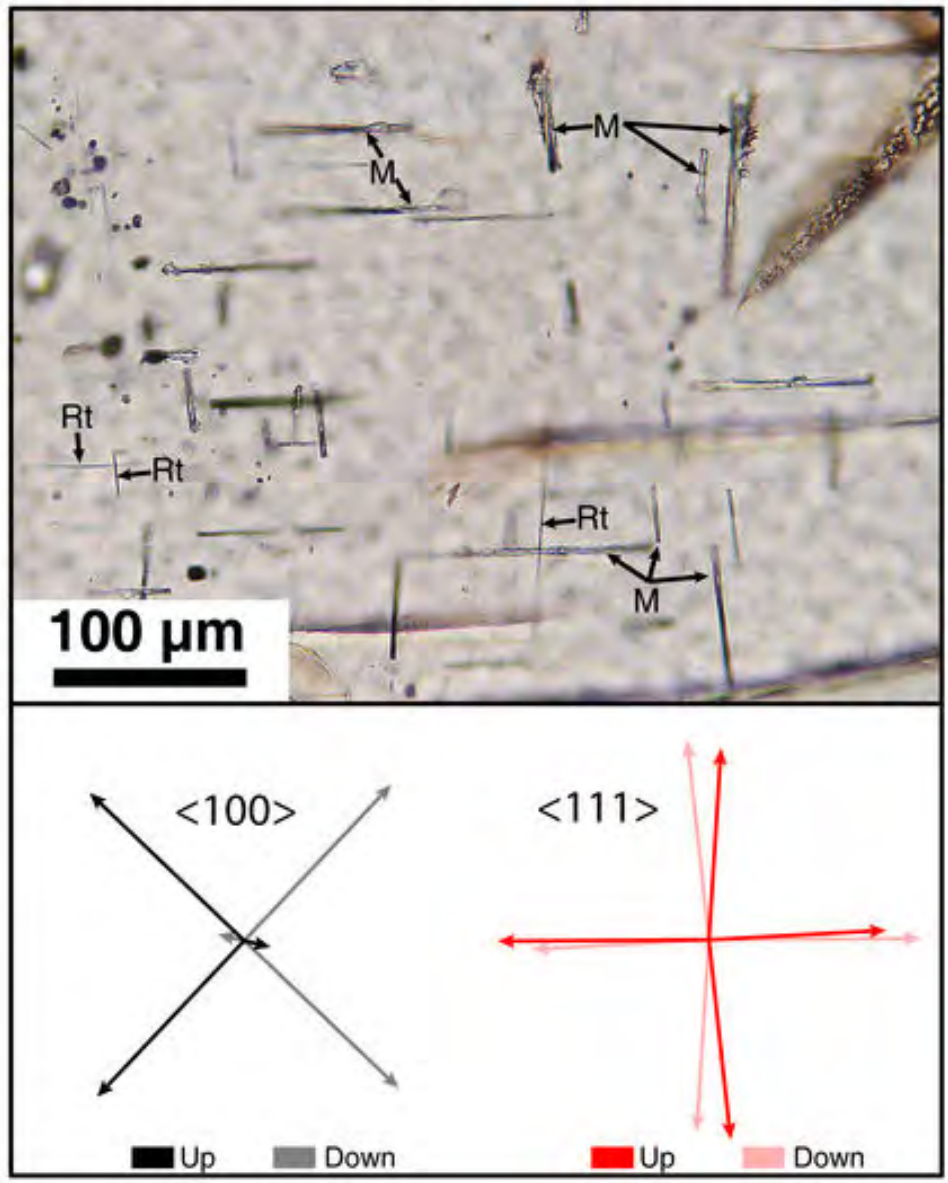

Figure 2. Axler and Ague

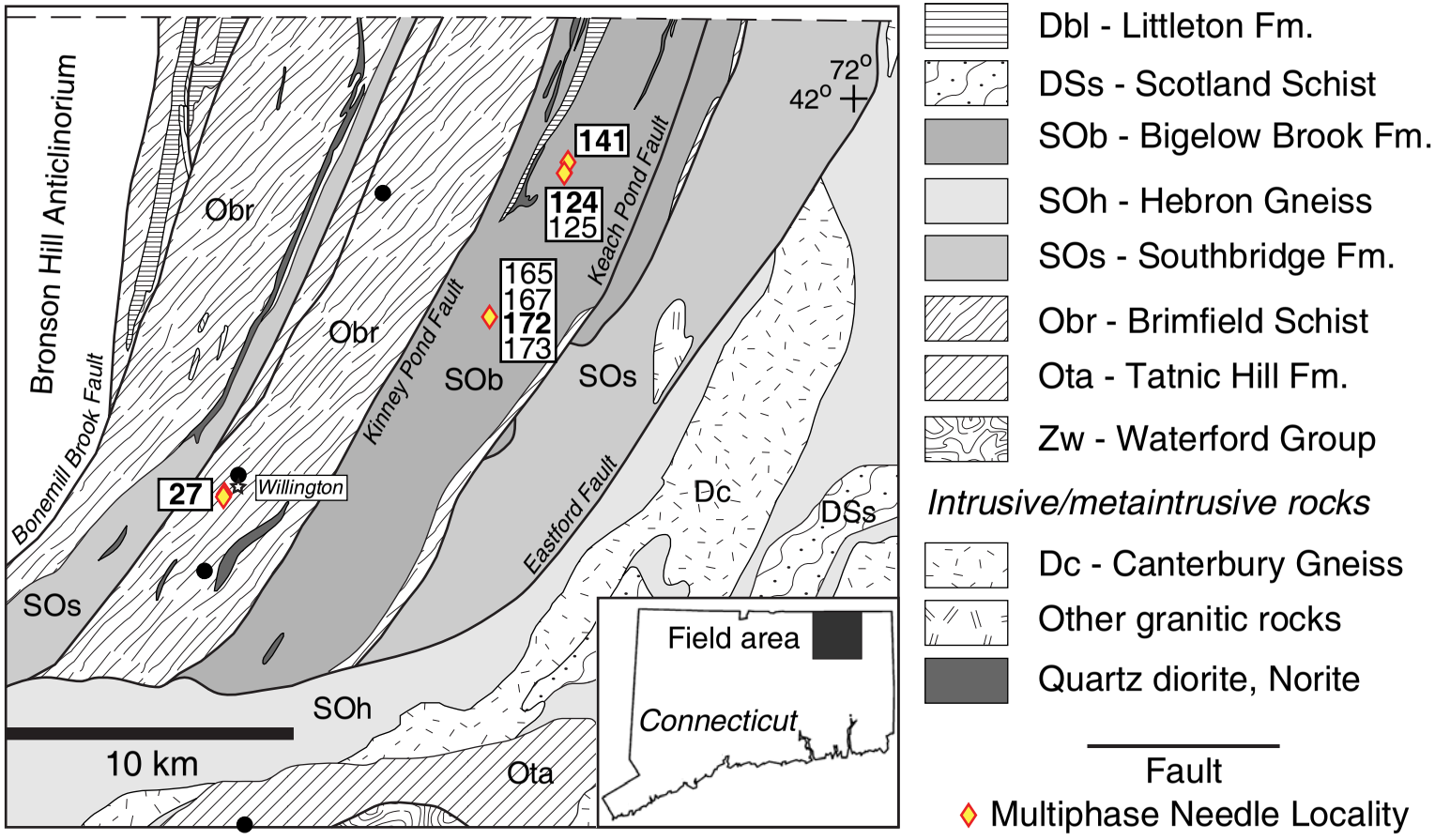

Figure 3. Axler and Ague

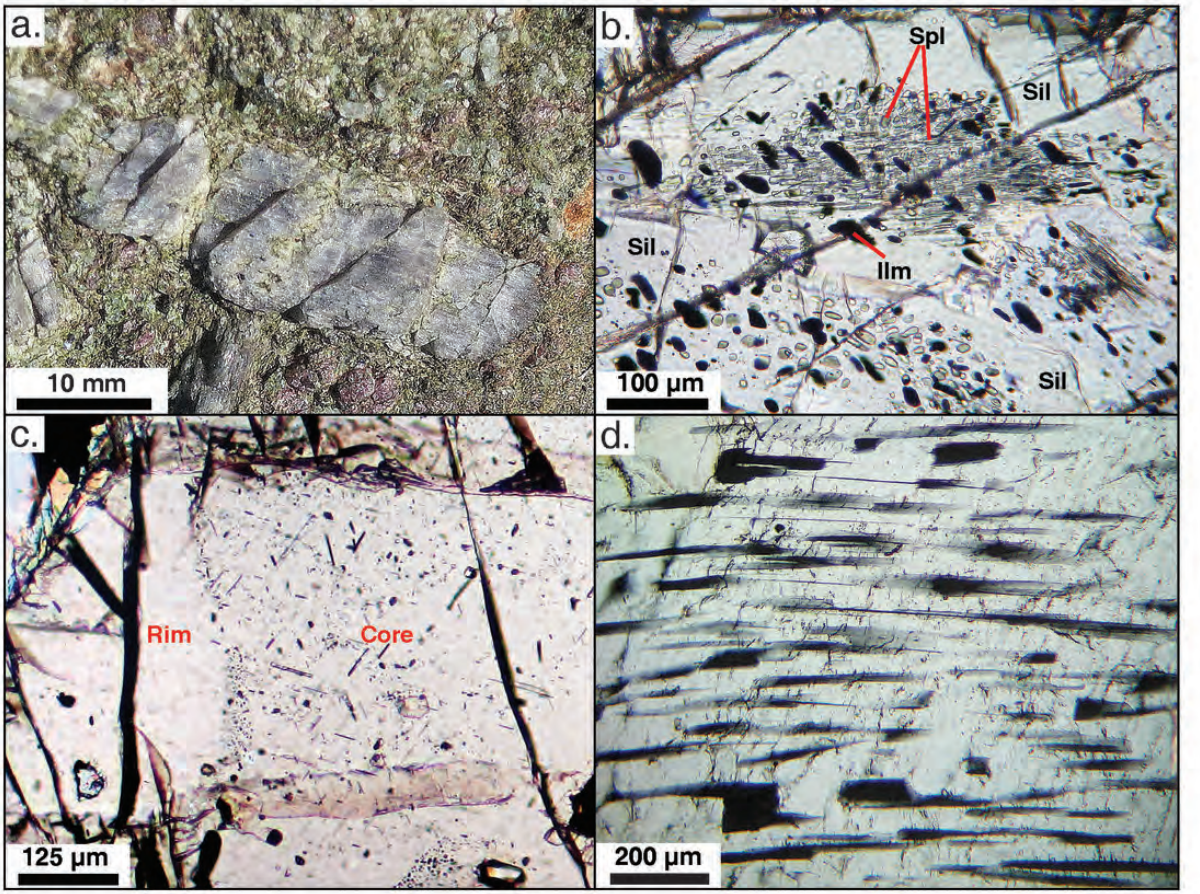

Figure 4. Axler and Ague

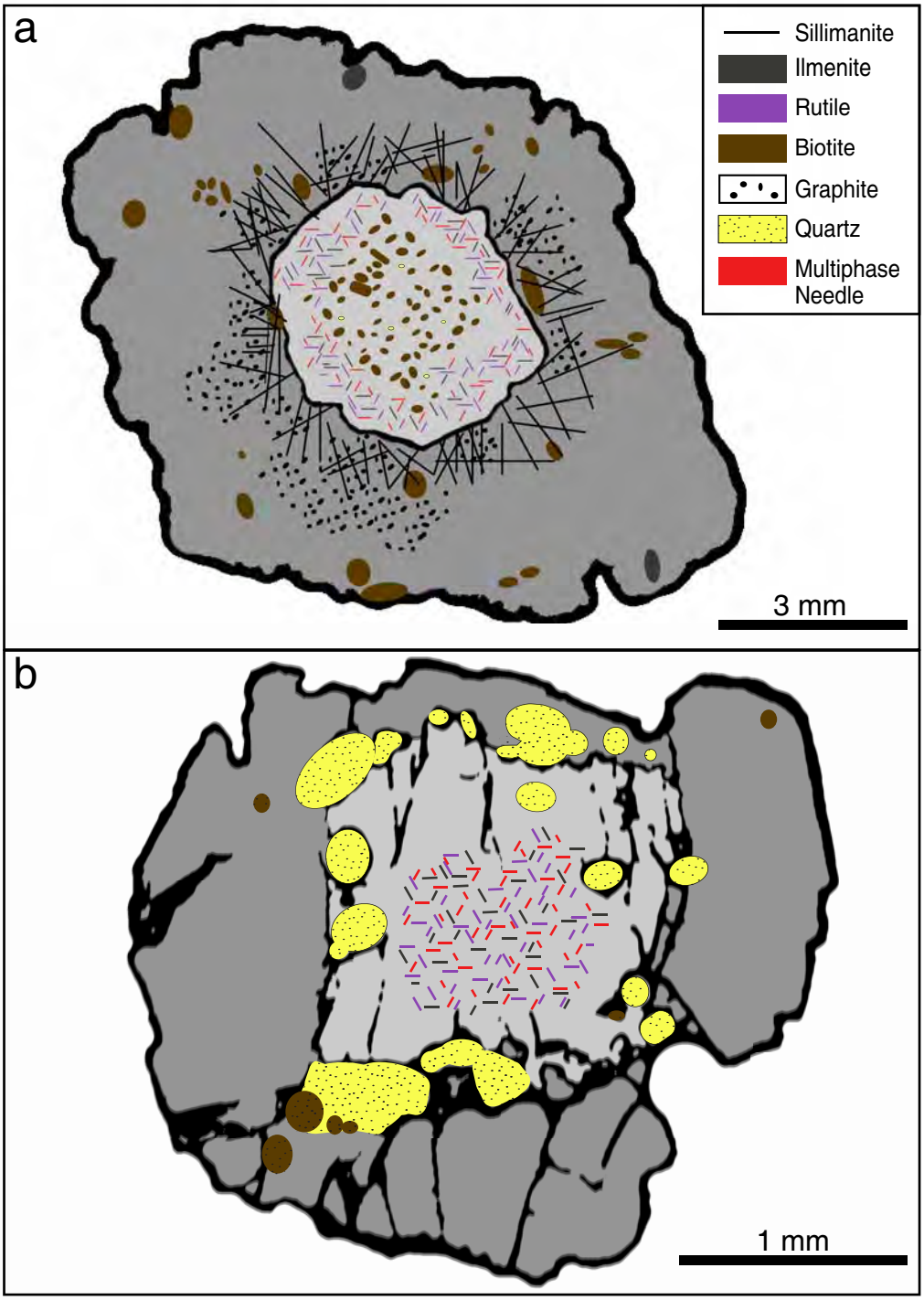

Figure 5. Axler and Ague

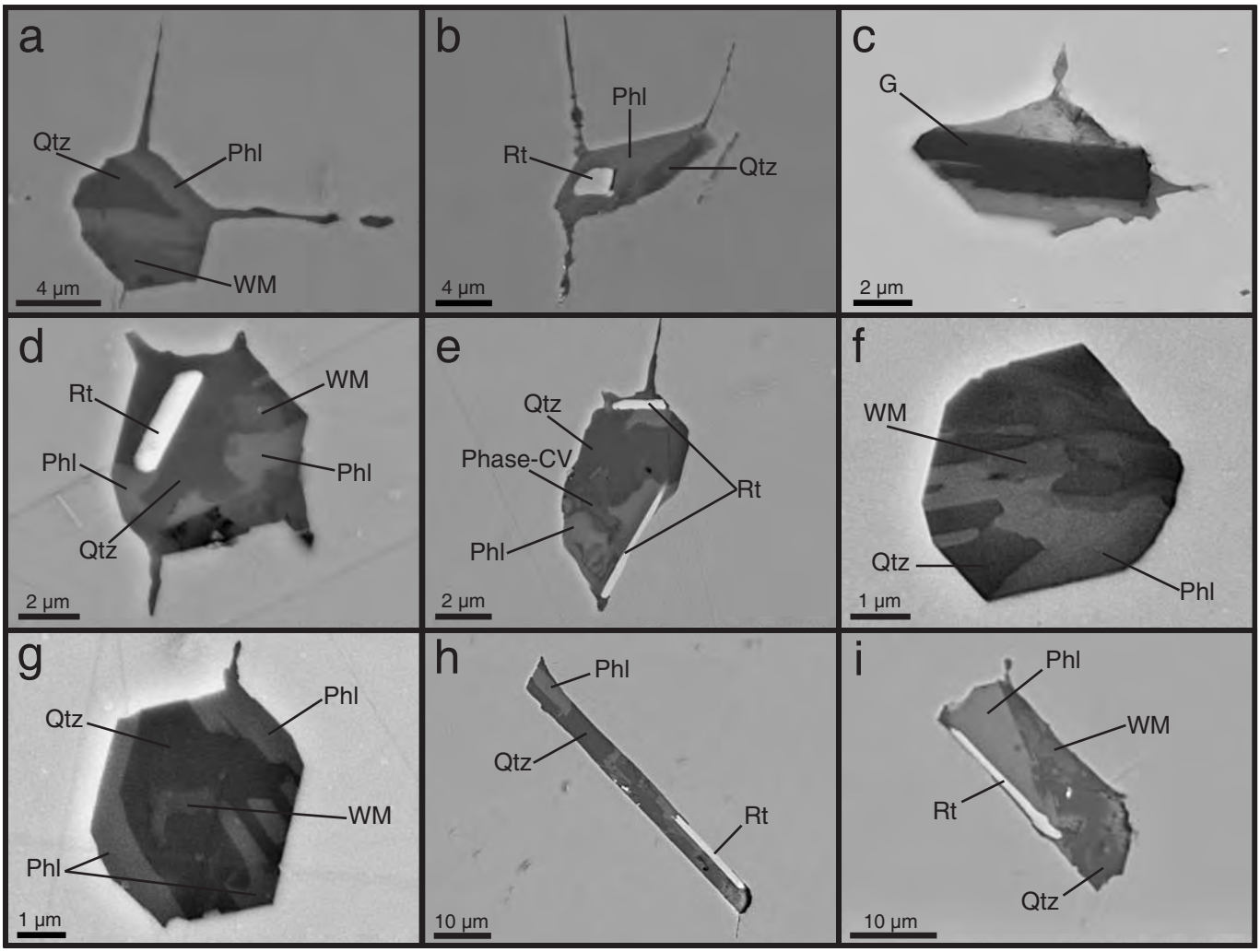

Figure 6. Axler and Ague

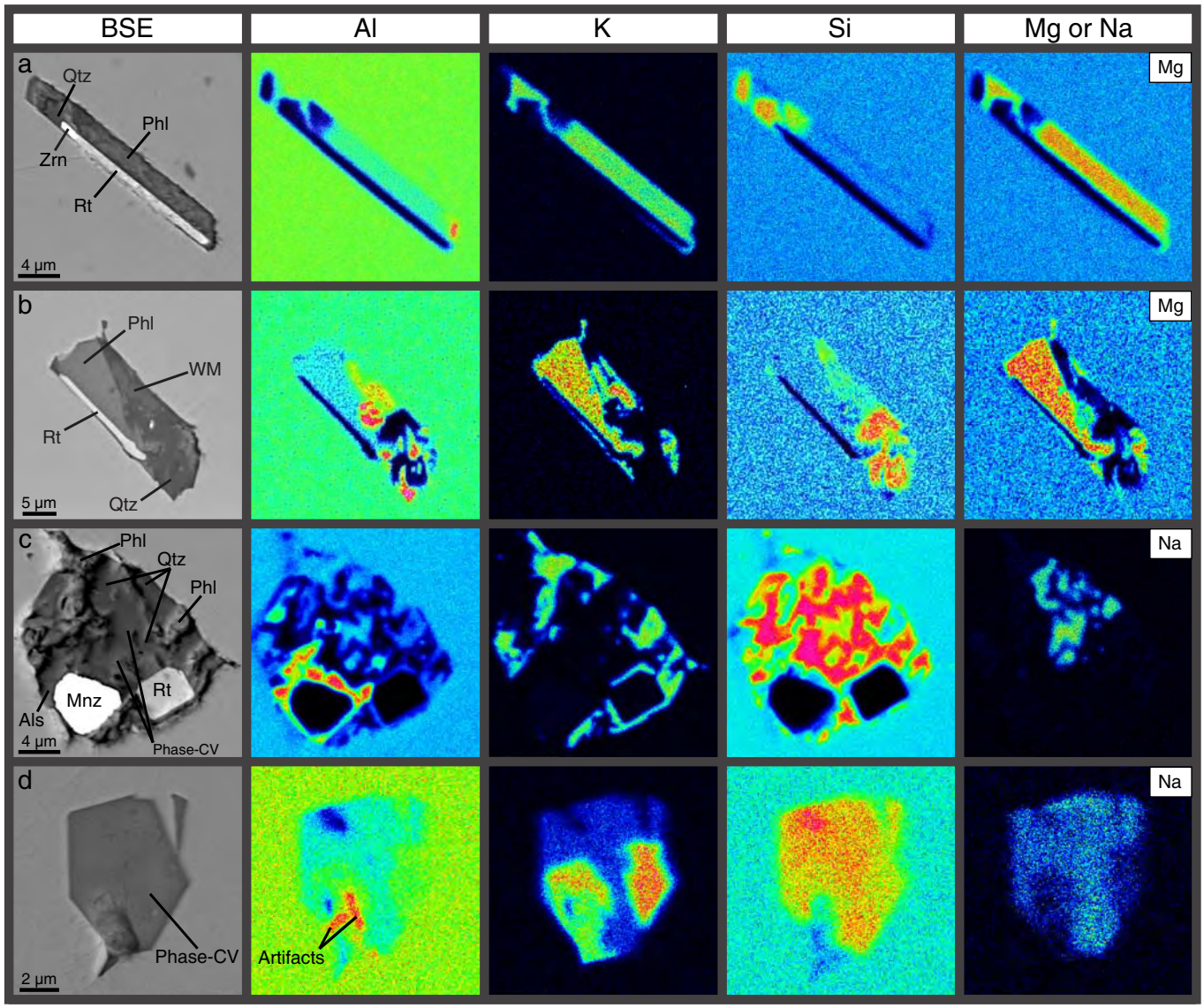

Figure 7. Axler and Ague

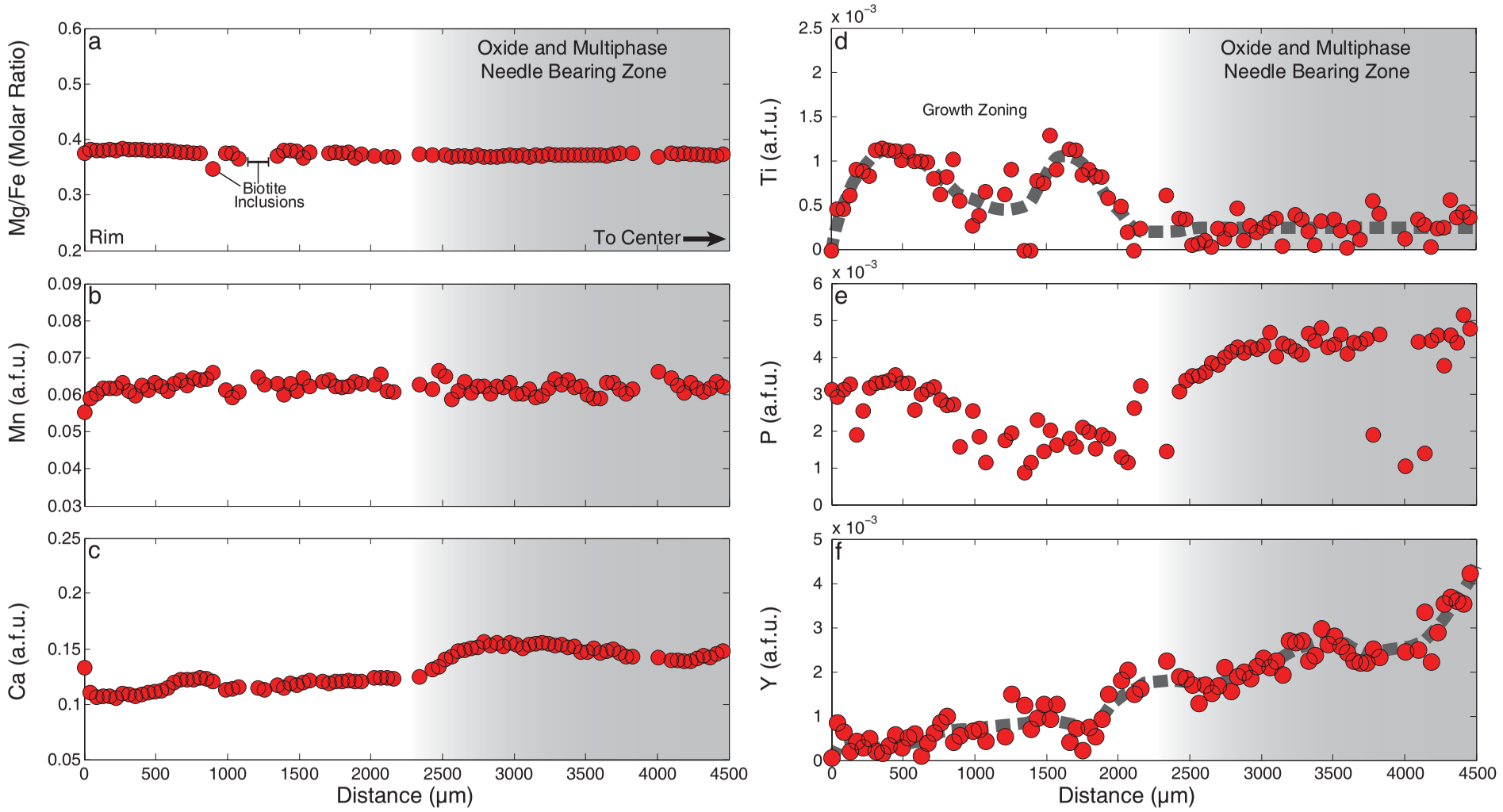

Figure 8. Axler and Ague

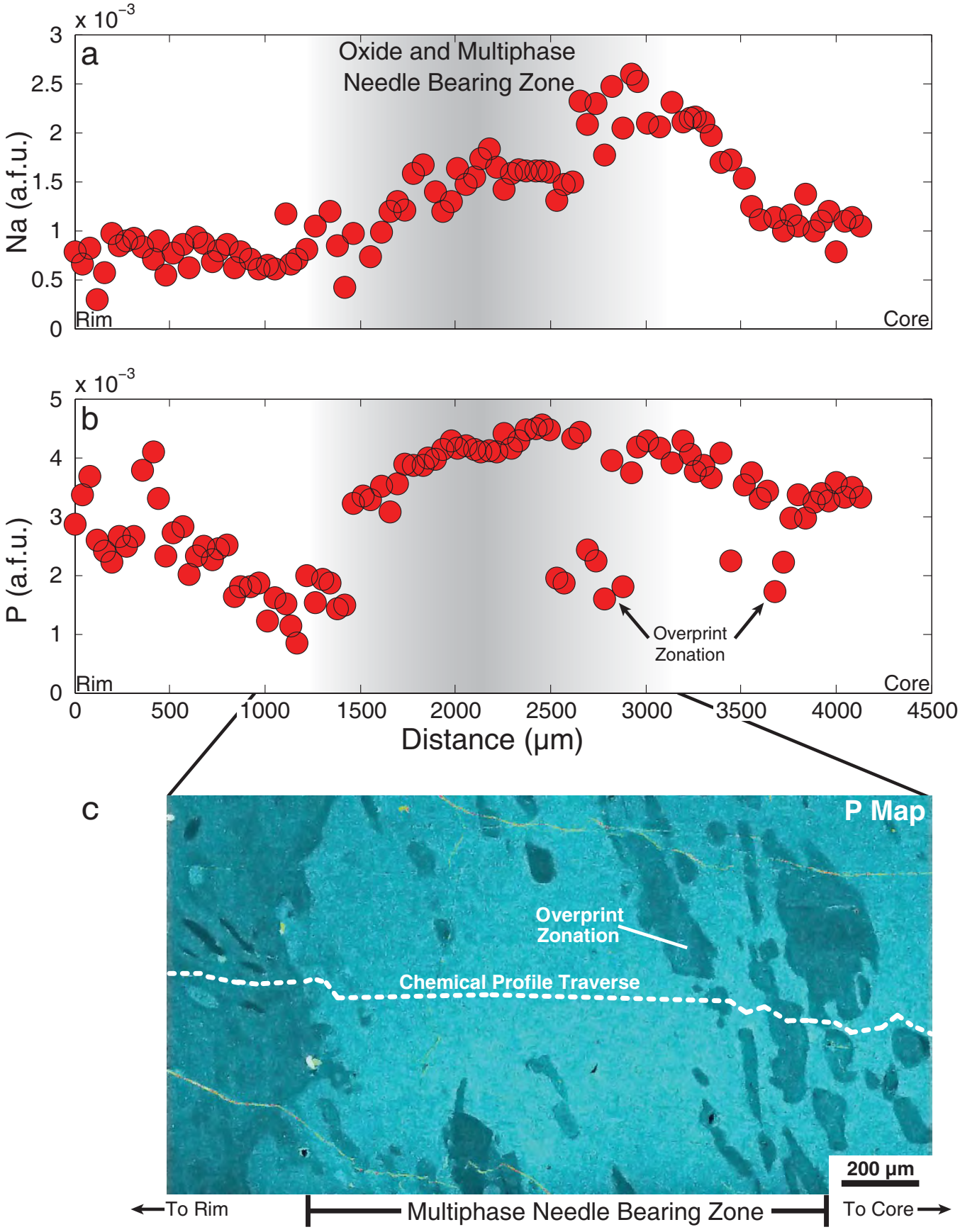

Figure 9. Axler and Ague

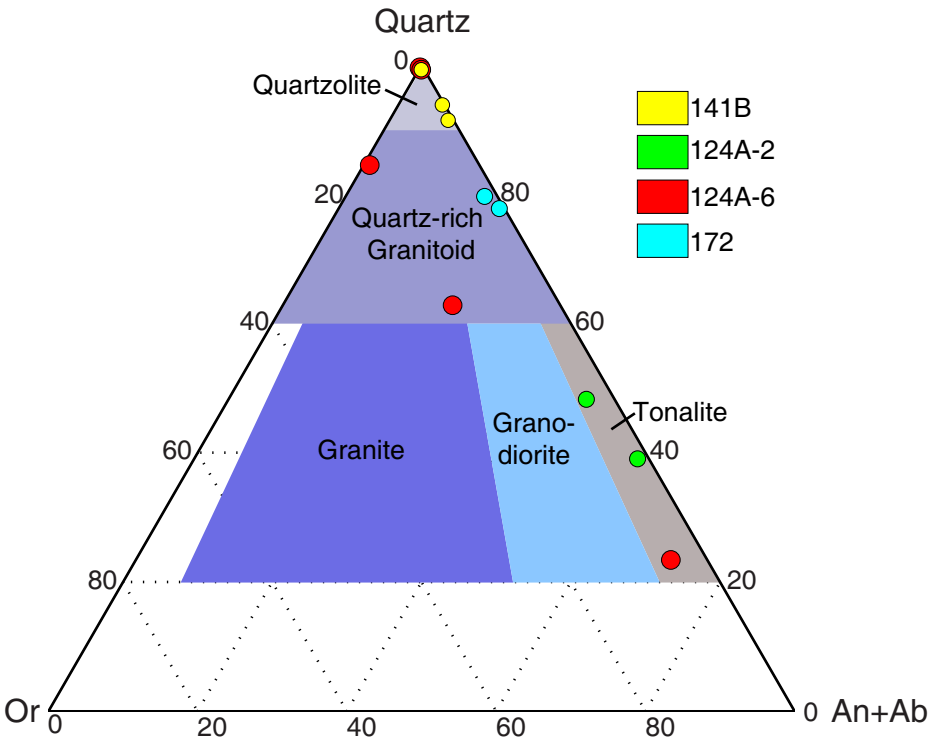

Figure 10. Axler and Ague

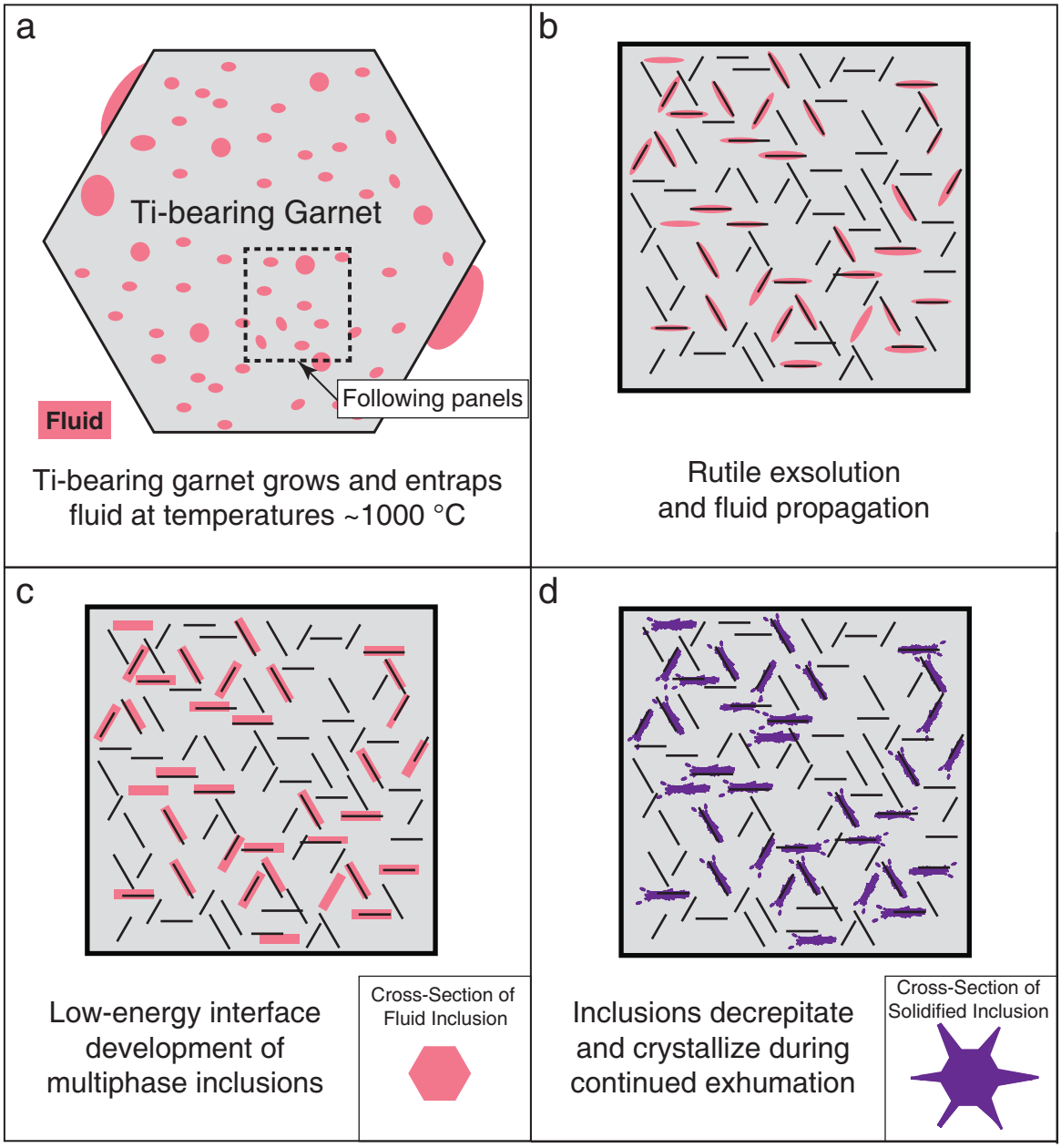

Figure 11. Axler and Ague

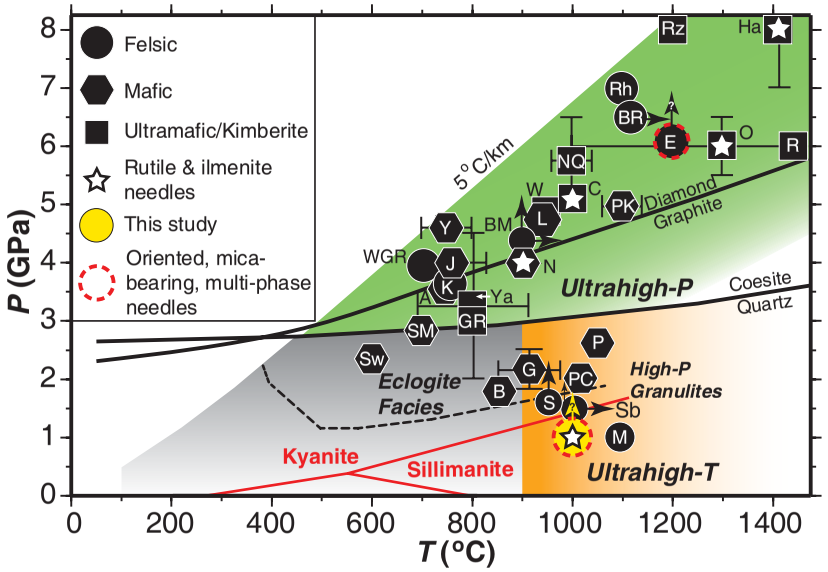

Figure 12. Axler and Ague